BRAGG COHERENT X-RAY DIFFRACTIVE IMAGING OF COEXISTING PHASES IN NANOPARTICLES: A SIMULATION STUDY

A Thesis

Presented to the Faculty of the Graduate School

of Cornell University

In Partial Fulfillment of the Requirements for the Degree of

Master of Science

by

Ziyi Wang

August 2019

ABSTRACT

Phase transformations are prevalent and play a profound role in energy density and rate capability in energy storage devices like batteries. Detecting the strain field at the nanoscale is one way to understand the phase transformation. Bragg Coherent diffractive imaging with phase retrieval algorithms is a possible candidate for imaging phase transformations. However, the current iterative algorithms fail to retrieve the images from X-ray data in the presence of large strains (~1%). By improving the phase retrieval algorithm, we show that Bragg coherent diffractive imaging of structural phase transformations in nanoparticles is possible. We verify our algorithm with reconstruction from simulated X-ray data.

BIOGRAPHICAL SKETCH

Ziyi Wang joined the Department of Materials Science and Engineering at Cornell University in August 2017. He is working in Professor Andrej Singer's group, and he mainly works on the simulation of the Bragg coherent X-ray diffractive imaging. Ziyi has participated in experiments at several synchrotron light sources including the Cornell high energy synchrotron source (CHESS) and the advanced photon source (APS).

Before coming to Cornell University, Ziyi got his Bachelor of Engineering degree in Materials Science and Engineering field at Peking University.

ACKNOWLEDGMENTS

I sincerely thank my advisor, Prof. Andrej Singer, for all his help in my two-years study. He inspires me to improve as a researcher in the materials science field. He also provides me with much knowledge and skills, which will benefit me in my future research career.

I am also very grateful to other collaborators of this project, Prof. Veit Elser and Dr. Oleg Gorobtsov. Prof. Elser enlightens me by providing much advice, and Oleg helps me a lot in practice and details. I would not be able to accomplish this project without their support.

I also deeply appreciate my Professors at Cornell University, including Prof. Lena Fitting Kourkoutis, Prof. Richard Douglas Robinson, Prof. Chekesha Liddell Watson, and other helpful professors. Prof. Kourkoutis is my committee member and helps me a lot in finishing my thesis. Prof. Robinson gives me great assistance in researching different energy storage nanomaterials. Prof. Watson is helpful in teaching and solidifies my materials science background. It is my fortune to receive help from all these kind professors.

I would also like to thank other group members, including Ziming Shao, Daniel Weinstock, Ryan Bouck, Wenxuan Qiu, Yifei Sun, Jiaruo Li: it is a great pleasure to work in this group and help with each other.

I want to give special thanks to my parents, Mr. Daqing Wang and Mrs. Haoyun Yin, for their timely encouragement and unconditional love. I may not able to overcome the difficulties without their patience.

Finally, I would like to express my gratitude to Cornell University, especially to the Department of Materials Science and Engineering. Cornell University provides me with a peaceful environment for studying and numerous opportunities for practicing research. I have a great time here.

TABLE OF CONTENTS

CHAPTER 1

INTRODUCTION

1. Phase Transformations in Nanomaterials

With the rapid development of nanotechnology, nanomaterials find their applications in various fields including medicine[1], environment[2], optics[3]. Especially, because of the high surface area, porosity, and other properties of nanomaterials[4], scientists have been putting effort into applying these materials in energy-related applications, particularly including the batteries[4–7].

Although our method is applicable for any other functional nanomaterial, here we consider a concrete example: Li-ion batteries. Phase transformations are critical for batteries. Typically, in the cathode nanomaterials of the Li-ion batteries, the Li-ions move out of the cathode material during discharge, as shown in Figure 1, and intercalates back during charge. In some important cathode materials (such as nickel-manganese spinel and lithium iron phosphate), the transportation of these lithium ions leads to a phase transformation in the electrode nanomaterials.[4–7]

The nanosized spinel-$LiNi_{0.5}Mn_{1.5}O_4$ (LNMO) electrode is an example to illustrate the phase transformations in functional nanomaterials. Compared with other cathode materials, the LNMO cathode has advantages in high operating voltage, high rate performance, and potentially low cost.[8] These years, the nanosized LNMO is attracting more attention as scientists reveal that the shapes and sizes of electrodes are also closely associating with their electrochemical properties. Therefore, the nanosized

LNMO electrode is a possible choice for a high rate capacities and a good cycling performances of batteries.[8,9]

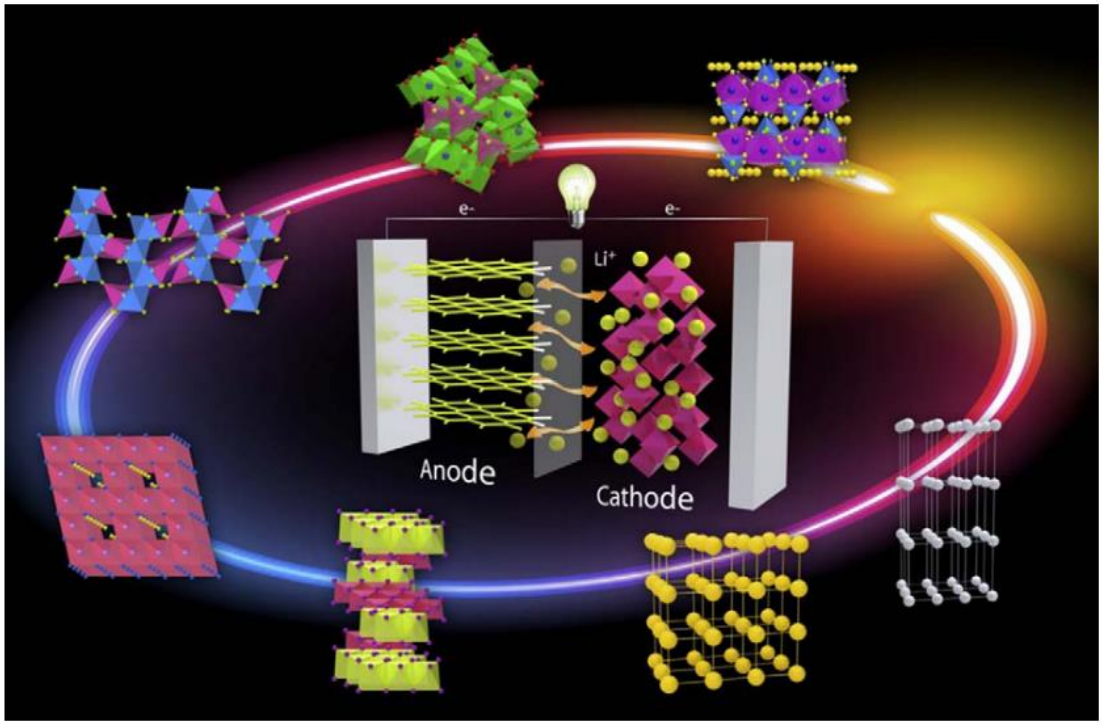

Figure 1. Schematic shows the basic composition of the Li-ion battery and the various of cathode materials with different structures. Figure adapted from Ref. 7.

There are two structures of LNMO material: the ordered $P4_332$ structure and the disordered $Fd\bar{3}m$ structure, which are both shown in Figure 2.[9] In both structures, the Li atoms and the O atoms locate in the same sites of the octahedral unit cell. The difference comes from the positions of Mn and Ni atoms. In the ordered $P4_332$ structure, the Mn atoms and Ni atoms respectively locate in the sites referred to as 4*b* and 12*d* in $P4_332$ structure. In the $Fd\bar{3}m$ structure, however, the Mn atoms and Ni atoms can randomly switch their positions.[10] Compared with the ordered $P4_332$ structure, the disordered Fd$\bar{3}$m structure has variations in the distances between sites

in the unit cell, and that is because of the difference in ionic radius between the Mn atoms and the Ni atoms.[9]

The difference in structures of the LNMO cathodes can impact the operation of the battery. Previous studies show that the disordered structure has better rate capability and better cycling stability, due to the faster Li^+ diffusion. Scientists have revealed that one fundamental reason for this high diffusion coefficient is the Mn^{3+}, which has a larger ionic radius compared with the Mn^{4+}. The appearance of the Mn^{3+} in the disordered structure expands the lattice and provides larger space for Li^+ transportation.[11]

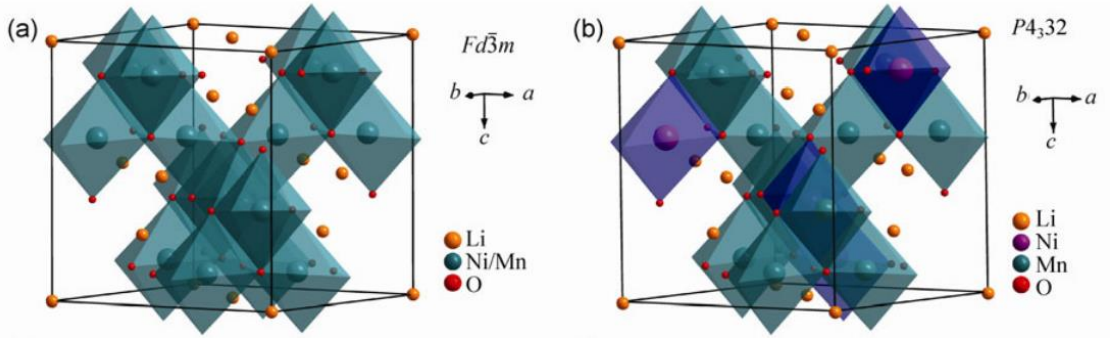

Figure 2. Schematic shows the structures of the disordered $Fd\bar{3}m$ structure (a) and the ordered $P4_332$ structure (b) of LNMO crystal. Figure adapted from Ref. 9.

The functional phase transformation of LNMO comes from the charging-discharging cycles. The charging reaction at the LNMO electrode is: [12]

$$LiNi_{0.5}Mn_{1.5}O_4 \rightarrow Li_xNi_{0.5}Mn_{1.5}O_4 + (1-x)\,Li^+ + xe^- \qquad (1)$$

Here, x is between 0 and 1. In the ideal charging process of the ordered LNMO, apart from the moving out of the Li^+, the Ni^{2+} partly turns into Ni^{4+}. In the disordered LNMO, however, there exist other reactions like part of the Mn^{3+} turns into the Mn^{4+}.[12]

In the charging process, the missing of the Li-ions and the valence change of Ni and Mn ions lead to structural phase transformations in this kind of cathode electrode. Previous studies show that when the x in the reaction mentioned above changes from 1 to 0, the lattice constant correspondingly changes from around 8.16 Å to 8.00 Å.[12–15]

Ideally, this phase transformation is reversible in the discharging cycle. However, the capacity of the battery fades after several charge-discharge cycles. Possible reasons include the Mn dissolution and the active Li^+ loss. These side reactions also lead to phase transformations in the electrode structure.[16]

To better understand the structural phase transformation in nanomaterials, a possible way is detecting the lattice response. Strain is a good way to characterize the lattice response. According to the mechanic laws, the strain ε is defined as:

$$\varepsilon = \frac{\Delta l}{l_0} \tag{2}$$

Here, l_0 is the original length of the object, and Δl is the variation of this length.[17] When the length becomes longer, the strain is positive, and when the length becomes shorter, the strain is negative. In crystals, if the l_0 represents the lattice constant d_0, then the Δl is the displacement distance of the atomic planes Δd. Because the lattice

spacing varies between different phases, strain field then has different values in different phase regions. However, when the nanoparticle transform has two coexisting phase, there choice for the average lattice parameter d_0 is somewhat arbitrary; the nanoparticle is strain free at the beginning and the end of the phase transformation. In this thesis, we will calculate the strain $(d - d_0)/d_0$ with a fixed average lattice constant d_0 for the complete phase transformation process. The average lattice constant d_0 is the average between the lattice constants of the two participating structural phases and d is the local lattice constant imaged with BCDI.

Generally, in LNMO cathode, the strain varies from 10^{-2} to 10^{-4}.[9,13] The strain due to phase transformations during charge-discharge cycles has a magnitude around 10^{-2},[13] which is several magnitudes higher than the strain between the ordered LNMO and disordered LNMO. Therefore, in the nanomaterials, it is possible to determine the types of different phase transformations by detecting their typical strain fields.

2. Existing Methods Studying Phase Transformations

In order to capture the lattice response, scientists have developed several techniques. One commonly used method for characterizing the crystal lattice is X-ray diffraction (XRD).

X-ray is electromagnetic radiation with energy of about 10 keV. Around 100 years ago, Bragg, Laue, and other scientists developed the basic equation for describing the elastic x-ray scattering [18]:

$$f(\boldsymbol{q}) = \int \rho(\boldsymbol{r}) \cdot e^{-i\boldsymbol{q}\cdot\boldsymbol{r}} d\boldsymbol{r} \tag{3}$$

Here, $f(\boldsymbol{q})$ is called as the *atomic form factor*, $\rho(\boldsymbol{r})$ is the electron density at the position $\boldsymbol{r}$, and $\boldsymbol{q} = \boldsymbol{k_f} - \boldsymbol{k_i}$ is the momentum transfer of the X-ray, and $\boldsymbol{k_i}$ and $\boldsymbol{k_f}$ are the incident and scattered wave vectors with $|\boldsymbol{k_f}| = |\boldsymbol{k_i}| = 2\pi/\lambda$ (λ is the wavelength of the X-ray). This structure form factor equals to the amplitude of the scattered X-rays. [18]

Due to the superposition principle, the light amplitude scattered from the crystal $F(\boldsymbol{q})$ is [19]:

$$F(\boldsymbol{q}) = \sum_j f_j(\boldsymbol{q}) \cdot e^{-i\boldsymbol{q}\cdot\boldsymbol{r}_j} \cdot \sum_n e^{-i\boldsymbol{q}\cdot\boldsymbol{R_n}} \tag{4}$$

In this equation, the first sum on the right is referred to as the *unit cell structure factor*, and the second sum on the right is the sum over the lattice. $f_j(\boldsymbol{q})$ is the atomic form factor of the *j*'th atom in the unit cell, which is generally approximating as a constant in the crystal, and $\boldsymbol{r_j}$ is its position within each unit cell. $\boldsymbol{R_n}$ is the lattice vector to determine the position of the *n*'th unit cell.

According to equation (4), in the simplest situation, where $j = 1$, $F(\boldsymbol{q})$ reaches a maximum when $\boldsymbol{q} \cdot \boldsymbol{r_j}$ is a multiple of 2π. Therefore, the Bragg's law or Laue's condition conclude this relationship as [19]:

$$2d\sin\theta = n\lambda \quad \text{or} \quad \boldsymbol{q} = \boldsymbol{h} \tag{5}$$

In this equation, d is the distance between two atomic planes, θ is the scattering angle, and n is a positive integer. $|\boldsymbol{h}| = 2\pi/d$, and its direction is perpendicular to the atomic plane. This relationship is illustrated in Figure 3. When the optical path difference between the beam 1 and 2 shown in Figure 3 is $n\lambda$, the two scattered beams have the same phase angle in the light amplitudes, and this doubles the total light amplitude. When the Bragg condition is met, a signal with high intensity is observed on the detector, resulting in powerful methods such as X-ray powder diffraction[19,20].

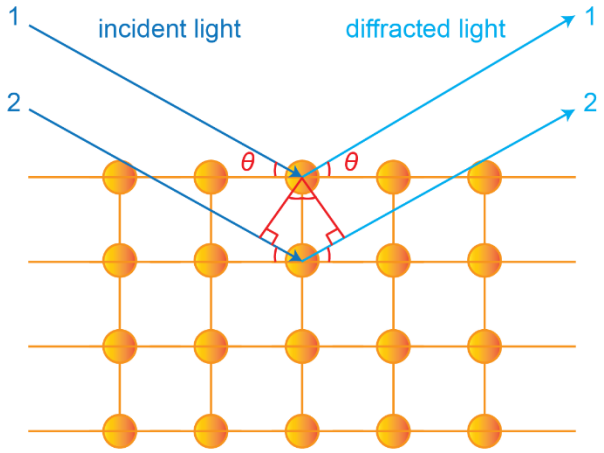

Figure 3. The illustration of X-ray diffraction under Bragg's condition.

Based on the previous laws like equation (5), scientists developed the powder X-ray diffraction method. In this method, the sample consists of small powder. Therefore, the orientations of lattice are distributed in all directions. When fixing the incident X-ray beam, the scattered light intensity reaches the maximum once the scattered angle meets the Bragg's law for the particles in the correct orientation. For a large number of particles are present in the sample the Bragg condition is always true for some particles. This method enables scientists to detect multiple interatomic distances existing in the unit cell with a single scan.

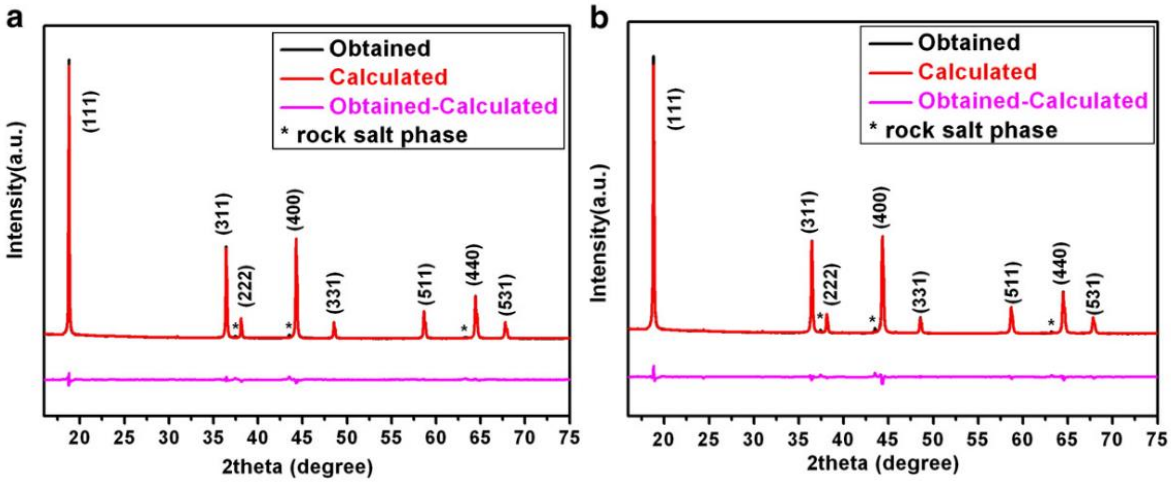

Figure 4. The powder X-ray diffraction0 result of the disordered $Fd\bar{3}m$ LNMO crystal (a) and the ordered $P4_332$ LNMO crystal (b). Figure adapted from Ref. 13.

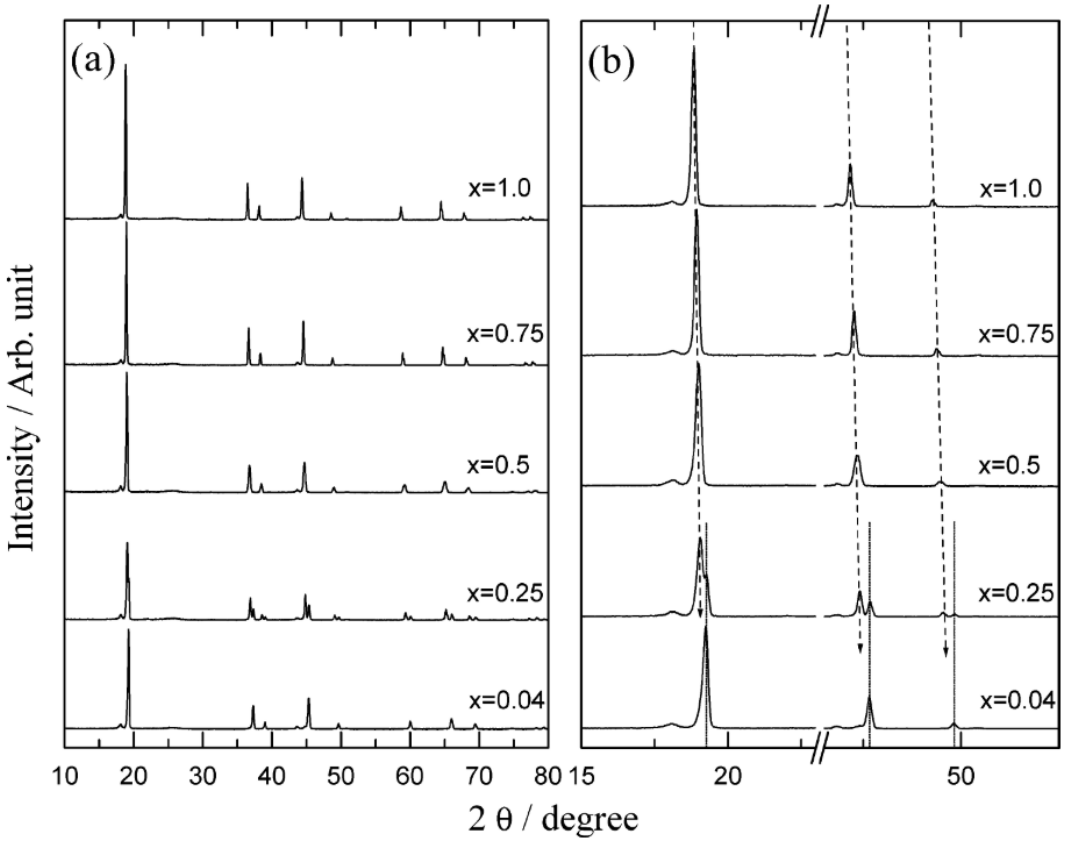

Figure 5. The *ex-situ* powder X-ray diffraction result of the disordered $Fd\bar{3}m$ LNMO crystal at different states of charge. Figure adapted from Ref. 12.

Powder x-ray diffraction is widely used in detecting various kinds of lattice change. As an example of detecting the small strain, Figure 4 shows the powder diffraction result of the disordered $Fd\bar{3}m$ LNMO crystal and the ordered $P4_332$ LNMO crystal. By analyzing the data, these scientists determine the lattice constant **a** as 8.1713 Å and 8.1688 Å for the disordered structure and the ordered structure respectively.[13]

For high strain situations, powder X-ray diffraction is also applicable. Figure 5 shows the *ex-situ* powder diffraction result of the phase change in the disordered $Fd\bar{3}m$ LNMO electrode during charging. The shifting of Bragg peaks shows the changes in lattice constant correspond to the phase transformations.

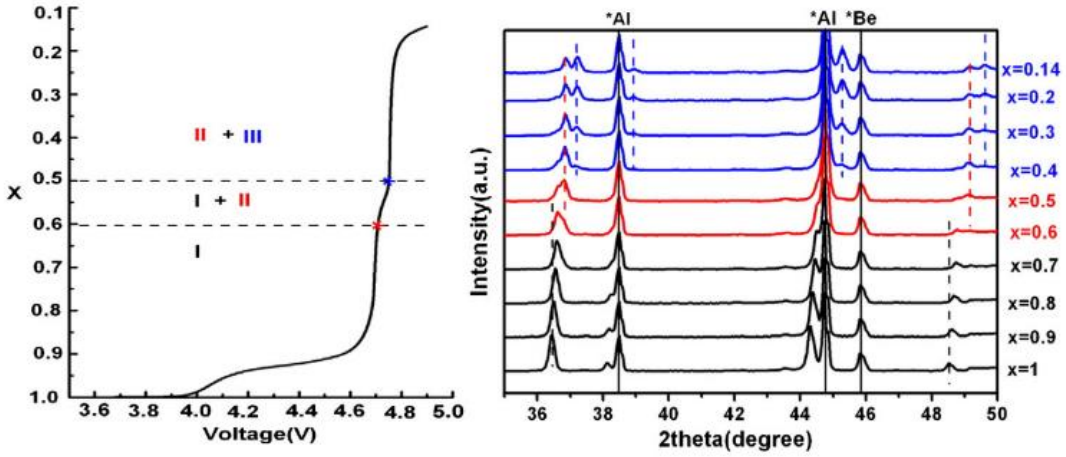

Figure 6. The *in-situ* XRD result and the corresponding charge-discharge curves of the disordered $Fd\bar{3}m$ $Li_xNi_{0.5}Mn_{1.5}O_4$ cathode. Figure adapted from Ref. 13.

An advantage of the X-ray diffraction method is the ability of *in-situ* measurements. As the X-rays can penetrate fully functional multi-component devices, and the interaction between cathode materials and X-ray does not disturb the operation of the

battery, it is possible to collect real-time data of the structural change in the cathode materials during the charge-discharge cycles.

Figure 6 shows the *in-situ* XRD result and the corresponding charge-discharge curves of the $Li_xNi_{0.5}Mn_{1.5}O_4$ cathode. Compared with the *ex-situ* data shown in Figure 5, the *in-situ* data maintains high accuracy. From this data, scientists conclude that there are three phases emerging in the charge-discharge cycles, which are shown in Figure 7. The lattice constant of these three phases are respectively 8.16 Å (phase Ⅰ), 8.08 Å (phase Ⅱ) and 8.00 Å (phase Ⅲ). The phase transformations happen while x=0.4 (phase Ⅰ to phase Ⅱ) and x=0.6 (phase Ⅱ to phase Ⅲ).[13]

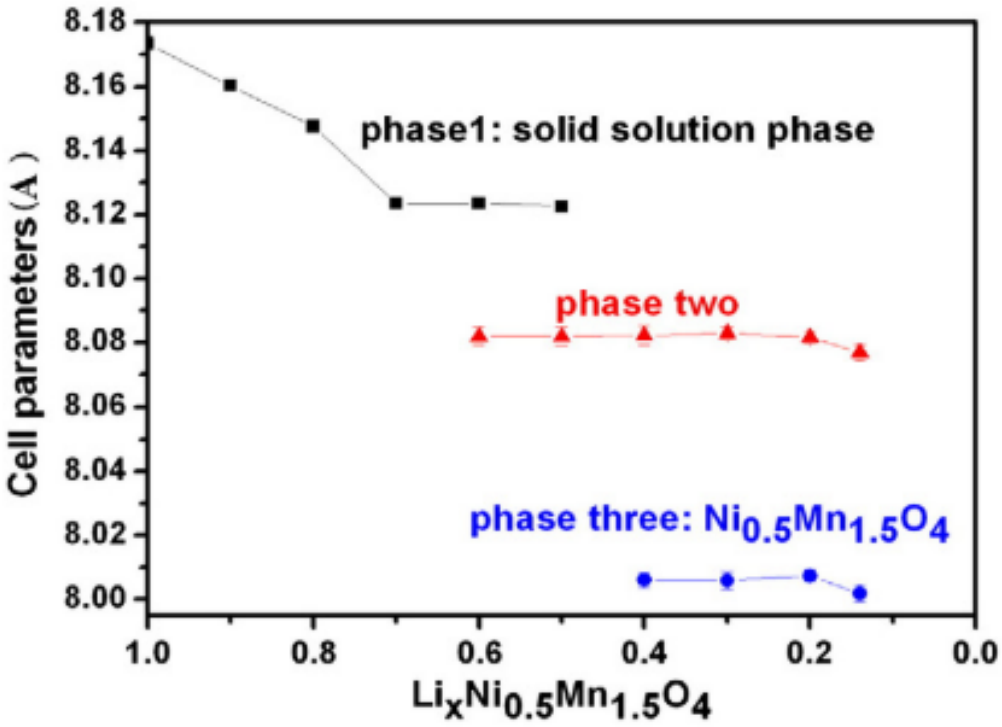

Figure 7. The different phases emerging in the charging process of the disordered $Fd\bar{3}m$ $Li_xNi_{0.5}Mn_{1.5}O_4$ cathode. Figure adapted from Ref. 13.

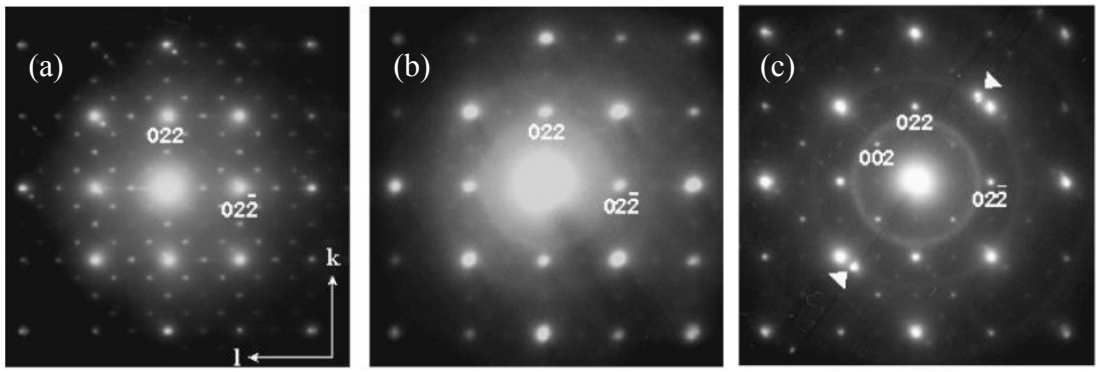

Figure 8. The electron different pattern of the ordered $P4_332$ $Li_xNi_{0.5}Mn_{1.5}O_4$ cathode. x = 1, 0.5 and 0.04 in (a), (b) and (c). The comparison between (a), (b) & (c) shows phase changes. Figure adapted from Ref. 12.

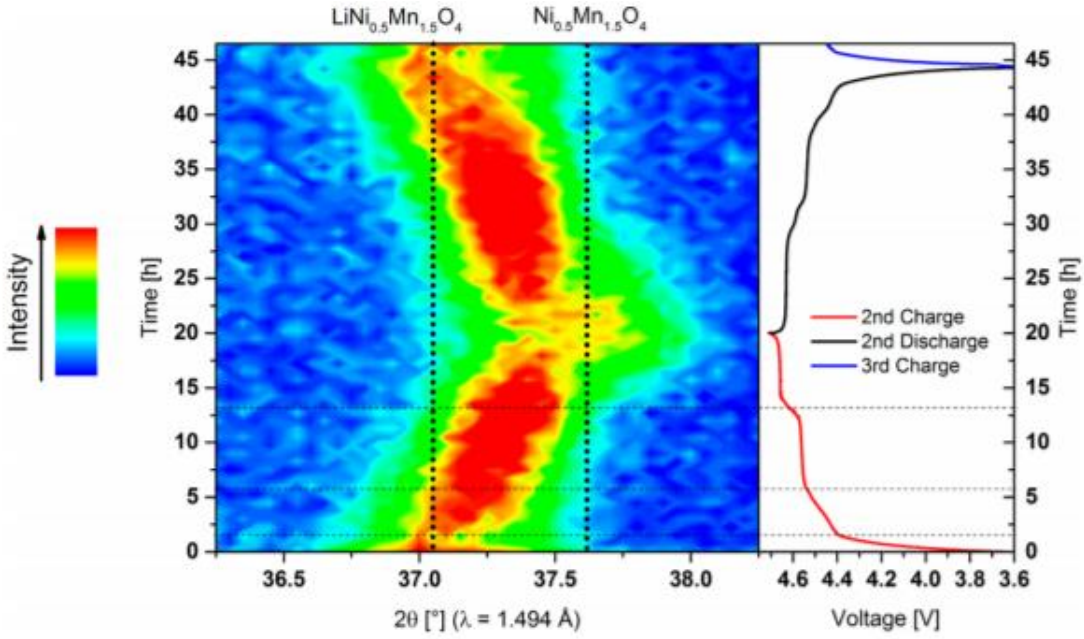

Figure 9. The *in-situ* neutron diffraction data and the corresponding charge-discharge curves of the (222) peak of the disordered $Fd\bar{3}m$ $Li_xNi_{0.5}Mn_{1.5}O_4$ cathode. [21] The shifting of the peak represents the lattice constant changes during charging and dischaging, and this lattice change is caused by phase transformation. Figure adapted from Ref. 19.

Other characterization methods for studying phase transformations in nanomaterials include electron diffraction[12], electron microscopy[9,12], neutron diffraction[19], and other possible methods. Figure 8 shows an example of the electron diffraction data, and Figure 9 shows an example of the neutron diffraction result of the average of a large volume of nanomaterial.

Although very powerful, traditional powder XRD only accesses average properties of the whole sample. Accessing a specific nanoparticle through conventional XRD is impossible. Therefore, scientists are still seeking for a possibility to image the real-time lattice response of a single nanoparticle with high resolution *in-situ*. With the development of the synchrotron light sources, Bragg coherent X-ray diffractive imaging becomes a possible choice.

3. Bragg Coherent X-ray Diffractive Imaging

The challenges in collecting *in-situ* data from single nanoparticles arise from several parts. First, if the source is unable to emit enough number of photons per unit time, the diffraction pattern is too noisy to distinguish the details. Second, to focus on nanoparticles embedded in a device, the incident beam size and the divergence of the incident beam need to be both low enough. Third, scientists need to decrease the bandwidth of the X-ray for collecting sharp diffraction data. The definition of *brilliance* concludes these requirements[20]:

$$\text{Brilliance} = \frac{\text{number of photons/second}}{(\text{mrad})^2(\text{mm source area})^2(0.1\%\ \text{bandwidth})} \qquad (6)$$

Brilliance is the parameter for characterizing the quality of the X-ray source. For the rotating anode X-ray source, which is generally used for powder XRD, the magnitude of its brilliance is around 10^8.[20]

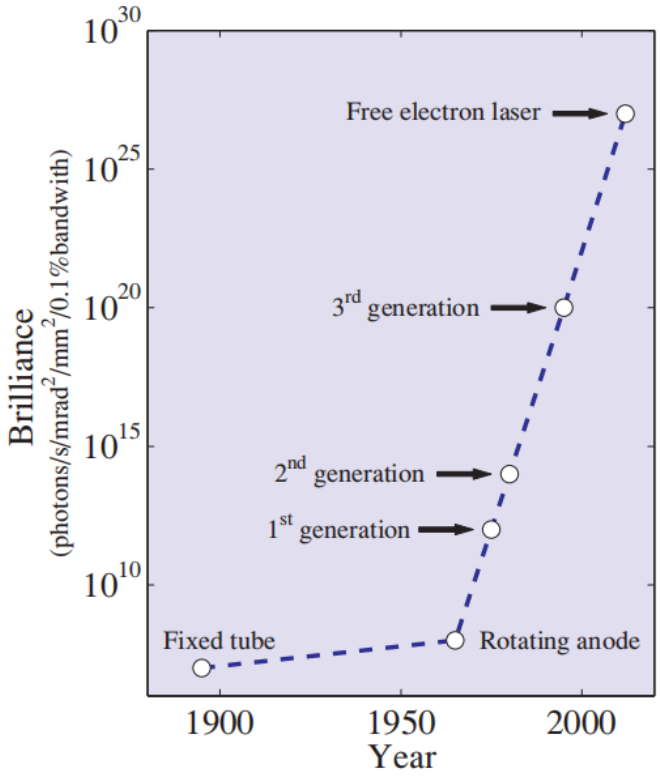

Figure 10. The history of the X-ray sources development and the brilliance improvement. Figure adapted from Ref.20.

In the past few decades, with the development of synchrotron light sources, the brilliance of the modern X-ray source is now several magnitudes higher than that of the rotating anode source. For example, the 3rd generation synchrotron light source, including ESRF (European Synchrotron Radiation Facility), APS (Advanced Photon Source) and SPring-8, can achieve a brilliance in the magnitude of 10^{20}. The

improvement of brilliance is shown in Figure 10, and now, with a high brilliance X-ray source, the high-resolution X-ray characterization methods become possible.[20]

Bragg Coherent Diffractive Imaging (BCDI) is a technique developed in recent years by the group of Ian Robinson,[21] and it is powerful in characterizing strain inside crystalline nanoparticles. By applying straightforward approximations on equation (4), the coherent x-ray scattering amplitude from a single nanoparticle can be written as[18]:

$$A(\boldsymbol{Q}) = \int s(\boldsymbol{r}) e^{-i\cdot 2\pi \boldsymbol{h}\cdot\boldsymbol{u}(\boldsymbol{r})} e^{-i\boldsymbol{Q}\cdot\boldsymbol{r}} d\boldsymbol{r} \qquad (7)$$

Here, $\boldsymbol{Q} = \boldsymbol{q} - \boldsymbol{h}$ and $\boldsymbol{q}$ is the scattering momentum transfer and $\boldsymbol{h}$ is the reciprocal space vector (see section 1.2). The shape function $s(\boldsymbol{r})$ is defined equal to 0 outside the nanoparticle and equal to 1 inside the volume of the nanocrystal. The displacement field at position $\boldsymbol{r}$ is denoted by $\boldsymbol{u}(\boldsymbol{r})$. This equation provides a connection between

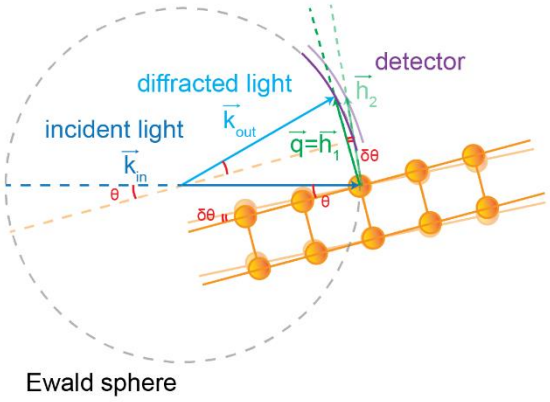

Figure 11. Schematically shows the experimental geometry of BCDI. Through rocking the crystal one maps out the 3D reciprocal space by moving it through the fixed Ewald sphere, mapped out by a 2D detector.

the 3D displacement field inside the nanoparticle and its corresponding 3D diffraction light wave.[18]

Compared with the strain field mentioned in equation (2), the displacement field is another way to characterize the lattice response, but they are related with each other. One can calculate the strain along the $\boldsymbol{h}$ direction by $\varepsilon_{\boldsymbol{h}} = du_{\boldsymbol{h}}(r_{\boldsymbol{h}})/dr_{\boldsymbol{h}}$, where $r_{\boldsymbol{h}}$ is the coordinate along the reciprocal space vector $\boldsymbol{h}$, and $u_{\boldsymbol{h}}$ is the displacement resolved along $\boldsymbol{h}$.

Figure 11 shows the experimental geometry of BCDI in the reciprocal space. In an experiment, diffraction data is collected by a fixed two-dimensional detector, which maps out a portion of the Ewald sphere in Figure11. This detector locates in the position of a Bragg peak, where $\boldsymbol{q} = \boldsymbol{h}$ and $\boldsymbol{Q} = \boldsymbol{0}$. Compared with the sample-detector distance, the detector is so small that the Ewald sphere portion is covers can be approximate as flat and collecting diffracted light perpendicular to the scattered light vector $\boldsymbol{k_{out}}$. Then we slightly rock the sample with a small angle $\delta\theta$, and thus $\boldsymbol{h}$ also shifts with the angle $\delta\theta$. At this moment, $|\Delta\boldsymbol{Q}| = |\boldsymbol{q} - \boldsymbol{h_2}| = |\boldsymbol{h}| \times \delta\theta$, and $\Delta\boldsymbol{Q}$ is along the direction of scattered light vector $\boldsymbol{k_{out}}$. This $\delta\theta$, also known as the angle step, is generally around 0.002° and the entire measure span is around 0.1°. Therefore, rocking the sample enables us to collect a series of paralleled 2D diffraction patterns, and we can combine them together for a 3D diffraction intensity in the reciprocal space mapping.[22]

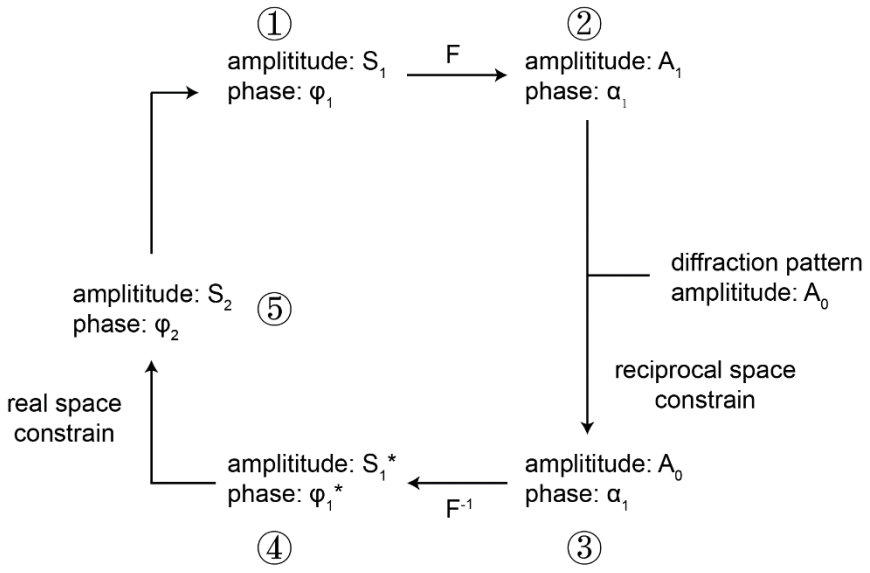

Figure 12. Schematically shows the general working process of phase retrieval algorithms.

In equation (7), the information of the nanoparticle is contained in the diffraction light wave. However, the detector can only receive the intensity of the light, which is the square of the light amplitude. In this case, the phase angle of the light wave is missing, and thus, key information is lost. In order to retrieve this information from the light intensity, phase retrieval algorithms become necessary. Therefore, this phase retrieval is a crucial step in BCDI; importantly phase retrieval only works if finite fringes due to x-ray coherence are present around the Bragg peak. With the development of coherent X-ray sources such as 3rd generation synchrotrons, detecting fringes with high accuracy became possible, which enabled BCDI.[18]

Multiple phase retrieval algorithms emerged in the past years. Gerchberg and Saxton introduced the first phase retrieval algorithm in 1972, called Error-Reduction (ER)

algorithm.[23] In 1982, Fienup invented another algorithm known as Hybrid-Input-Output (HIO) algorithm.[24] In the later years, scientists have developed more algorithms, including the Difference Map (DM) algorithm[25] and the Relaxed Averaged Alternating Reflection (RAAR) algorithm[26]. Figure 12 shows a general function process of the iterative phase retrieval algorithms.

The first step is giving a random guess as the initial start. In the second step, the algorithms apply Fourier transform on the initial start, as this realizes diffraction in equation (7). Then the algorithms replace the amplitude of the Fourier transformed data in reciprocal space by the real amplitude, and this step is known as the reciprocal space constraint. Next, the algorithms do inverse Fourier transform on the data in the reciprocal space and achieved new data in the real space. Finally, by applying real space constraint on the new real-space data, the algorithms acquire a new start, and they begin a new iteration of phase retrieval with this new start.

The main difference between different algorithms is real space constraint. For example, the real space constraint of the ER algorithms is:

$$S_2(\boldsymbol{r}) = \begin{cases} 0 \quad , & \boldsymbol{r} \notin \gamma \\ S_1^*(\boldsymbol{r}), & \boldsymbol{r} \in \gamma \end{cases}$$

Here, γ is the domain of definition of the real space.[24] Meanwhile, the real space constraint of the HIO algorithms is:

$$S_2(\boldsymbol{r}) = \begin{cases} S_1(\boldsymbol{r}) - \beta S_1^*(\boldsymbol{r}), & \boldsymbol{r} \notin \gamma \\ S_1^*(\boldsymbol{r}), & \boldsymbol{r} \in \gamma \end{cases}$$

Here, β is a constant between 0 and 1. Generally, for 2D retrieval, β is chosen as 0.8, while for 3D retrieval, β is chosen as 0.9.[24]

By using BCDI and phase retrieval algorithms, scientists have done several works on reshaping a single nanoparticle and have verified the result with SEM detection.[22,27] They have also determined the defects distribution in different nanoparticles by reconstructing their displacement fields.[28–30] BCDI is also capable for the *in-situ* detection of strain inside battery nanoparticles, including the LNMO cathode nanoparticles[31–33] and lithium-rich layered oxides[34].

Figure 13 shows the 3D reconstruction result of the LNMO nanoparticle from *in-situ* diffraction data. The nanoparticle in (b) shows a typical state of cathode nanomaterial in the charge-discharge cycle. There exist a negative strain field in the core part of nanoparticle, while there is a positive strain field on the surface of the nanoparticle. The negative and positive strain fields respectively refer to the compression and tension in the nanoparticle, which are caused by the poorness and richness of the Li-ions.[32,33]

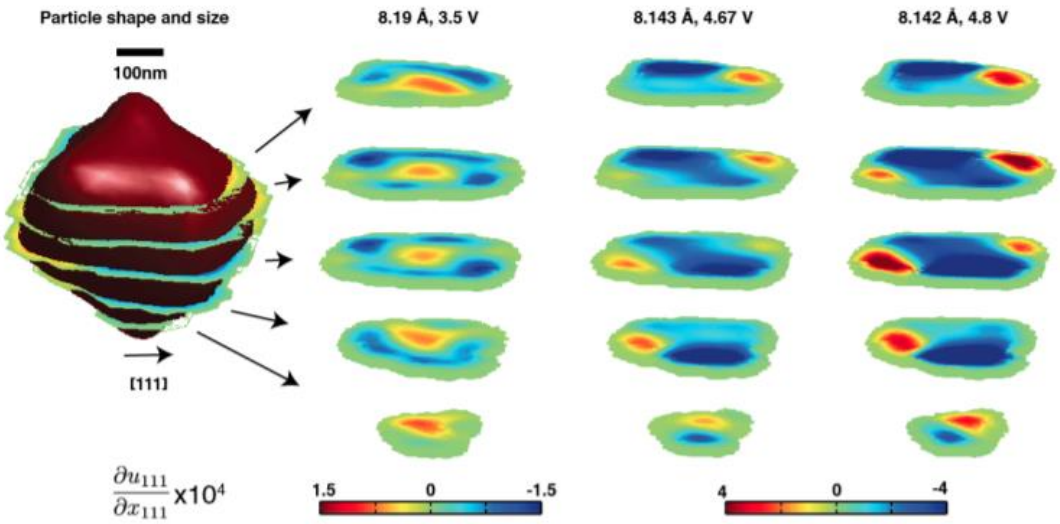

Figure 13. *In-situ* strain evolution of the LNMO nanoparticle. The shape of the reconstructed nanoparticle is shown in (a), and (b), (c) & (d) shows several slices of the nanoparticle at different states. Figure adapted from Ref. 33.

Figure 14 shows a series of (111) Bragg peaks of the LNMO cathode nanoparticles during the charge-discharge cycles. The shifting of the Bragg peak is similar to the powder x-ray diffraction data shown in Figure 7, but here diffraction from a single nanoparticle is recorded. In the charge cycle shown in (a), the original Bragg peak splits into two, and these two minor peaks and the middle fringes co-exist for a long time period, which refers to the mixing of the two phases. This mixing is a signature of a metastable solid solution. In the discharge cycle, however, the time is longer, and the middle fringes are not as strong as the charge cycle. This indicates phase separation during the slower phase transformation. These *in-situ* BCDI experiments provide scientists with evidence to study nonequilibrium structural dynamics in LNMO cathodes.[31]

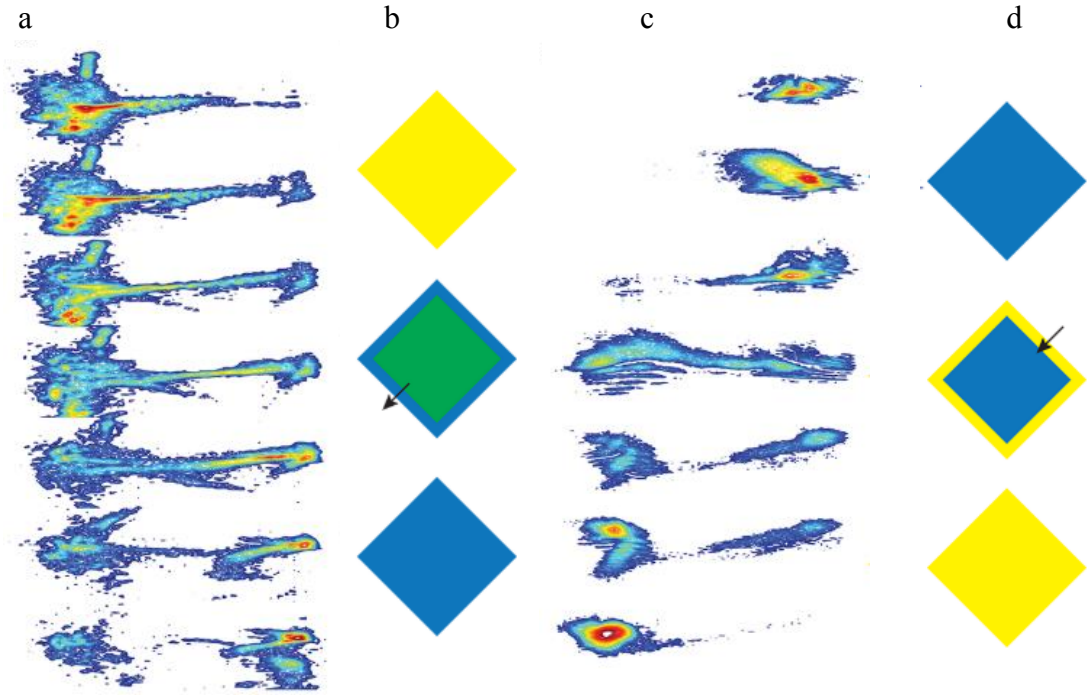

Figure 14. *In-situ* detection of the shifting (111) Bragg peak of the LNMO nanoparticle during the charge (a) and discharge (c) cycles. The vertical axis represents the time and the horizontal axis represents the diffraction angle. The corresponding phase transformation processes are briefly shown in (b) and (d). The yellow and blue color respectively represent two phases and the green color means the mixing phase. Figure adapted from Ref. 31.

Although BCDI was demonstrated to be a viable technique for studying strain in nanomaterials, it displays a few key challenges. In the BCDI method, the accuracy of the reconstruction result is strongly related to the number of photons produced by the synchrotron source, especially when the strain field is low. Therefore, in these low strain cases, the accuracy of the nanoparticle reconstruction results requires verifications when the numbers of photons change.

Another problem of the current BCDI method arises when the magnitude of the strain field is high and the Bragg peak splits into two, as shown in Figure 14. The magnitude of these strain fields is typically around 10^{-2}.[9,13] In these cases, however, the previous attempts to apply phase retrieval algorithms to data similar to Fig.14 fail.[35]

In conclusion, we propose studying phase transformations in the functional nanomaterials by measuring strain. We introduced current methods in capturing the lattice response, including powder X-ray diffraction and electron diffraction, which lack in-situ access to single nanoparticles. We propose the Bragg coherent diffractive imaging method and pointed out two existing problems of this method. These two problems are the main inspiration for this project. In the next chapter, we will use computational simulation with the MATLAB program to investigate the availability of BCDI for studying phase transformations.

CHAPTER 2

SIMULATING BCDI ON PHASE TRANSITIONS IN NANOPARTICLES

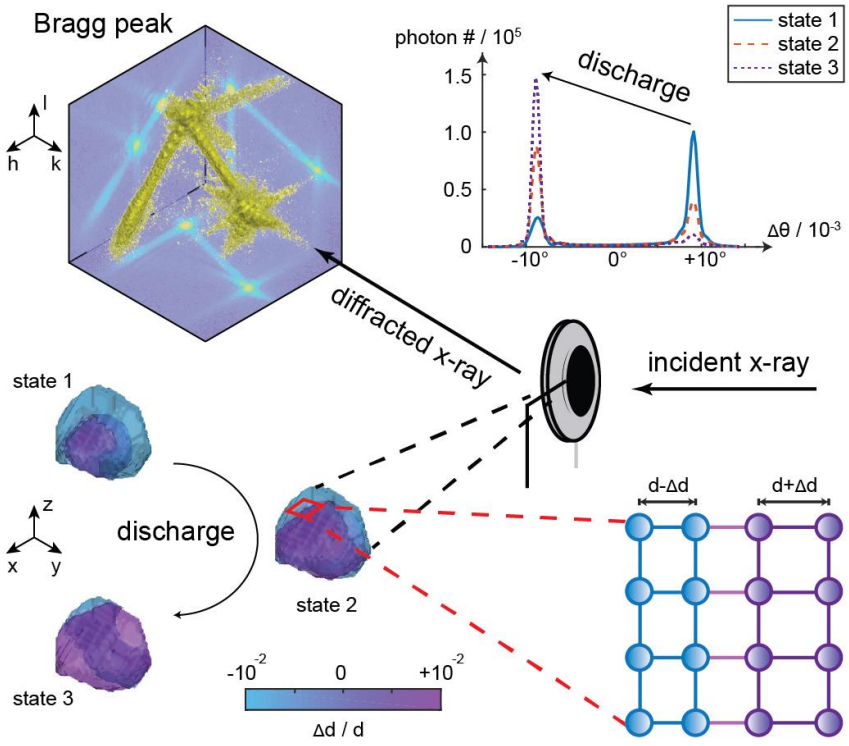

Figure 15. A schematic of the simulation of the BCDI experimental setup.

In this chapter, we will simulate the BCDI experiment on the nanoparticles undergoing phase transformations. Figure 15 illustrates our simulation. First, we simulate nanoparticles with two different phases, and we regard it as the electrode nanoparticle of the coin cell. Second, we simulate an incident X-ray beam on this nanoparticle, calculate its diffraction with Poisson noise, and throw out the phase angles. Third, we reconstruct the nanoparticle from this simulated diffraction data with traditional phase

retrieval algorithms. Finally, we evaluate the reconstruction results by comparing the reconstructed nanoparticle with the original one.

1. Building nanoparticles and simulating their diffraction data

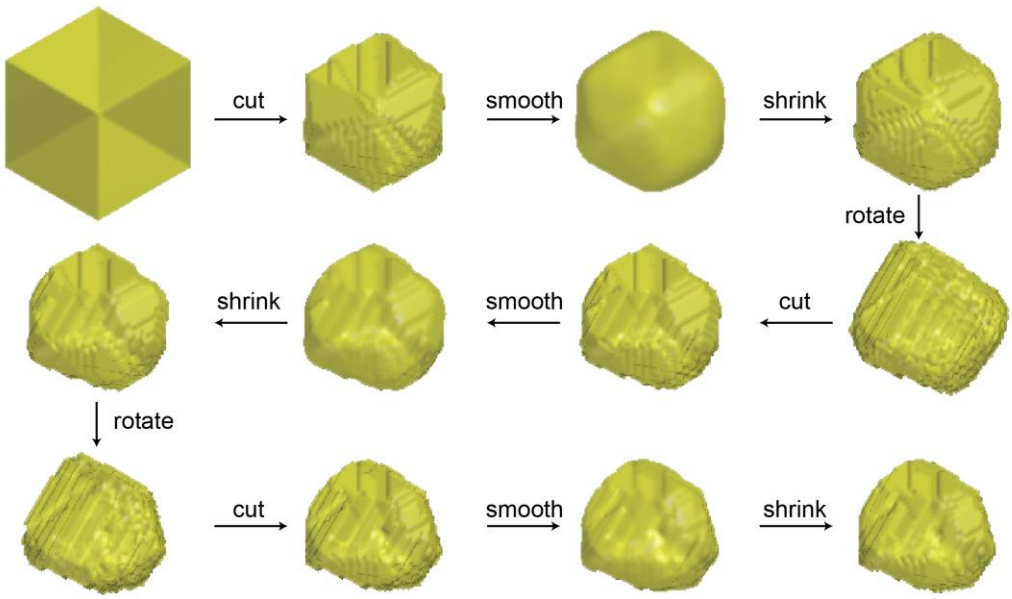

Figure 16. Illustration of the building process of the simulated nanoparticle.

We start by simulating a series of nanoparticles with random shapes by calculating their shape functions (see equation (7)). Figure 16 shows the general building process of simulated nanoparticle: we attempt generating irregularly shaped nanoparticles, which are found in a battery. First, we cut out a polyhedron from the space with 100 random planes. Second, we apply a smooth function on the inner polyhedron. Third, we shrink this nanoparticle by resetting its shape function to 0 and 1 with a threshold of 0.3. The smoothing and shrinking remove the sharp features at the corners and edges of the nanoparticle. Then we rotate this nanoparticle with a random angle and

repeat the above steps for two more times. This repeating increases the randomity of the nanoparticle.

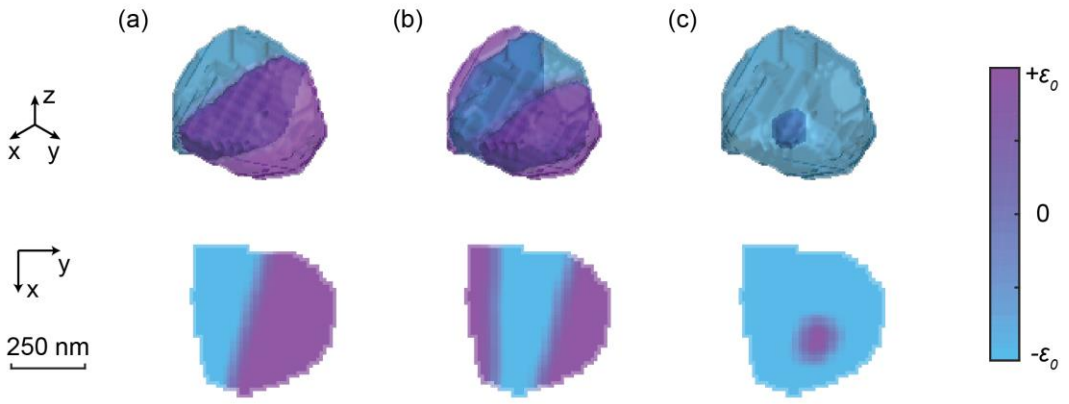

Figure 17. Simulated nanoparticle with different kinds of strain field distribution. Both 3D figure and the middle horizontal plane are shown. In (a) The new phase nucleates at the grain boundary and grows into the grain. In (b) nucleation occurs in two parts and grow into the grain. In (c) the new phase nucleates inside of the particle.

In the next step, we simulate the distribution of different strain fields. In Figure 17, we show three kinds of distributions of the strain fields simulated in this thesis. In Figure 17(a), we divide the nanoparticle with a randomly curved surface - the phase boundary - and distribute two different phases with a compressive strain field $-\varepsilon_0$ and a tensile strain field $+\varepsilon_0$, on two sides of the nanoparticle. Following the discussion in section 1.1, we calculate the strain from the average lattice constant, which is the mean value of the two lattice constants of the two structural phases. The phase boundary is the interface between the co-existing phases; we smooth this interface by several pixels to simulate the gradual change of lattice constant due to coherency strain.[36] The strain

field in Figure 17(b) is simulated with a similar method, and the only difference is that they have two interfaces. In Figure 17(c), we distribute two different phases with core-shell mode by simulating another smaller particle in the original one and giving the inner part and outer part different strain fields. We also smooth the phase boundary in this situation.

The three kinds of distributions in Figure 17 represent possible stages during different kinds of phase transformation processes. The phases in Figure 17(a) represent a moment during the phase transformation from left to right. Figure 17(b) can represent the phase transformation, starting from both sides of the nanoparticle. In Figure 17(c), the phase transformation starts from the interior of the nanoparticle.

The next step is calculating a displacement field with equation (7) from the simulated strain field. We pick the reciprocal space vector direction and calculate the displacement field by integrating the strain field by pixels along that direction. In our simulation work, we regard the *y*-direction as this direction, as shown in Figure 17. We assume that the middle *x*-*z* plane as the zero-displacement plane and verification experiment shows that adding constant displacement on the middle *x*-*z* plane does not change the result.

With the shape and the displacement field of the nanoparticle, we calculate the diffraction pattern according to equation (7). Then, we apply Poisson noise on this diffraction pattern to simulate the detection of the diffraction pattern in a rocking series by the 2D detector, as shown in Figure 11 and Figure 15. Because we saw no difference in the reconstruction results determined n using the experimental geometry and cartesian reciprocal space, in this thesis we used a cartesian coordinate grid in the

reciprocal space. The simulation result of the 3D Bragg peak of a typical nanoparticle is shown in Figure 18. Figure 18 demonstrates how the Poisson noise reduces the intensity of the fringes at the edge of the detector thereby reducing the resolution, which is roughly $2\pi/\Delta q$ where Δq is the distance between Bragg peak and the last visible fringe.

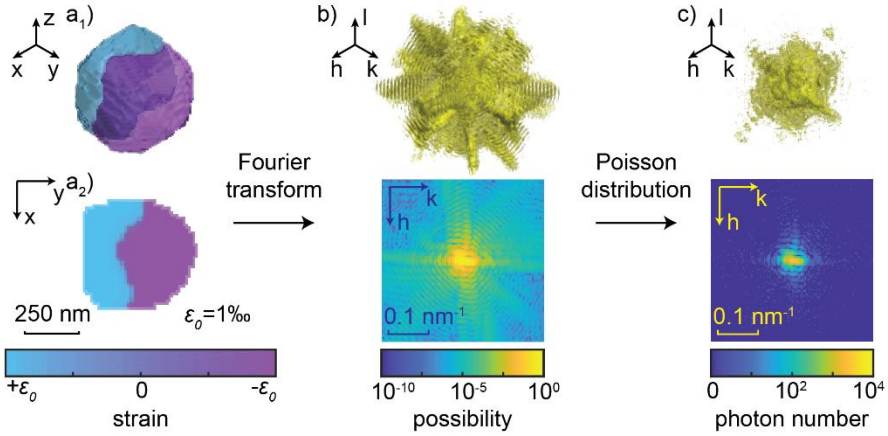

Figure 18. Illustration of the simulation process of the Bragg peak. The magnitude of strain ε_0 is 10^{-3}, and the total number of photons in the reciprocal space is10^6.

In our simulation work, the size of our simulated nanoparticles is around $(500\text{nm})^3$, similar to experimental sizes reported in Ref. 32. The size of the whole simulated real space is $(128\text{ pixel})^3$, corresponding to $(2\mu\text{m})^3$. We set the original lattice constant to 5 Å.

To simulate the X-ray diffraction experiments with different light sources, we change the number of photons from 10^4 to 10^8, while 10^6 is a current accessible photon number, and 10^8 is predicted for the future diffraction limited storage rings. We also set the energy of X-ray to 9keV, the diffraction angle 2θ to 15.85°, the sample-detector distance to 0.7984m, and the angle step $\delta\theta$ to ±0.004°. These parameters resemble real

experimental conditions in Ref. 32. The corresponding simulated XRD result with these parameters is shown in Figure 15.

The simulated diffraction patterns of the nanoparticle shown in Figure 18 in different conditions are shown in Figure 19. In this simulation, the magnitude of strain ε_0 varies from 10^{-4} to 10^{-2}, and we change the number of photons from 10^4 to 10^8.

As expected, with the increasing of the strain magnitude, as shown from left to right, the Bragg diffraction peak broadens and finally splits into two. The splitting follows directly from Bragg's law: the two coexisting phases have different lattice coefficients and diffract into different positions in the reciprocal space. When the peak separation becomes larger than the peak width, the peaks split. The latter is inversely proportional to the size of the respective phase region. Assuming that $n = 1$ ($d = d_0/n$ if not), by doing derivation on both sides of equation (5), we know that because of the $+\varepsilon_0$ and the $-\varepsilon_0$ in the nanoparticle, the diffraction angle changes:

$$2\Delta\theta = \frac{2\Delta d}{d} \cdot \frac{\lambda}{\sqrt{4d^2 - \lambda^2}} = 2\varepsilon_0 \cdot \frac{\lambda}{\sqrt{4d^2 - \lambda^2}} \tag{8}$$

Therefore, in the reciprocal space, the distance between the two peaks is:

$$2|\Delta Q| = 2\Delta\theta \cdot \frac{2\pi}{\lambda} = 2\varepsilon_0 \cdot \frac{2\pi}{\sqrt{4d^2 - \lambda^2}} \tag{9}$$

Take the parameters we set into equation (9). That is d as 5Å, and the energy of X-ray is 9 keV. Then we know the distance between the two peaks is: $2|\Delta Q|$ = 12.70 ε_0 nm^{-1} in our simulation. This distance $2|\Delta Q|$ is in proportion with the strain magnitude ε_0. Therefore, this distance in Figure 19a is 1.270×10^{-3} nm^{-1}, which is 10 times smaller

than the distance in Figure 19c and 100 times smaller than that in Figure 19e. In our simulation, 1 pixel in the reciprocal space is 3.149×10^{-3} nm^{-1}. Therefore, the center of the Bragg peak is not split yet when the strain magnitude ε_0 is 10^{-4}. The Bragg peak starts splitting when ε_0 is larger than $2.482\times10^{-4} = 10^{-3.605}$.

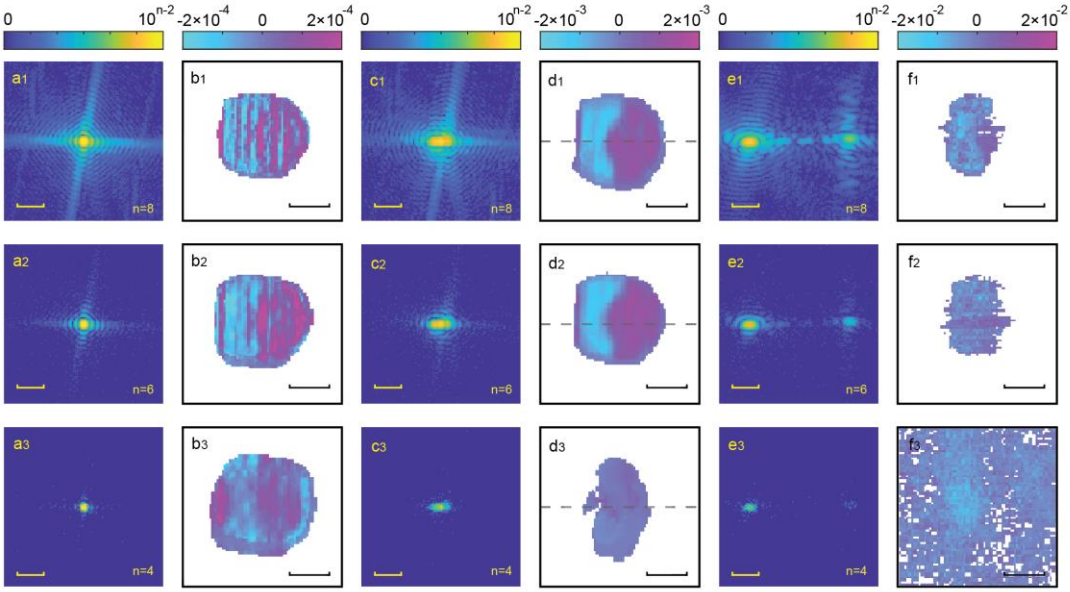

Figure 19. Images of simulated diffraction patterns and their corresponding reconstructed nanoparticles. The scale bar of real space is 250 nm and the scale bar of reciprocal space is 0.05 nm^{-1}. Column a, c & e show the diffraction patterns for nanoparticles with different magnitudes of strain fields of ε_0 as 10^{-4}, 10^{-3} & 10^{-2} while column b, d & f show their reconstruction results. Row 1, 2 & 3 show diffraction pattern with total photon numbers of 10^8, 10^6 &10^4 (represented as 10^n) in the whole reciprocal space and their corresponding reconstruction results. The magnitude of reconstructed strain is around ε_0, but sometimes higher or lower. Therefore, we show the reconstructed strain in the scale of $-2\varepsilon_0$ to $2\varepsilon_0$. The reconstruction higher than $2\varepsilon_0$ or lower than $-2\varepsilon_0$ are respectively patterned as $2\varepsilon_0$ and $-2\varepsilon_0$, because all these parts are considered unreliable.

From top to bottom, the secondary peaks or fringes, which contain the information of the shape and the strain, gradually disappear as the number of photons decrease. Counting fringes along one direction in reciprocal space, the number of visible fringes is more than 10 if we collect 10^8 photons in total, but this number drops to around 7 when the photon number is 10^6 and is less than 2 when the photon number is 10^4. According to equation (7), the distance between the fringes is $2\pi/L$, and L is the size of the nanoparticle. As the resolution of BCDI is around $2\pi/\Delta q$ where Δq is the distance between Bragg peak and the last visible fringe, the resolution decreased from less than $0.1L$ to around $0.5L$ with the number of photons decreasing. Meanwhile, because of the Poisson noise, the signal-noise ratio, equaling to $\sqrt{10^n}$, also decreases with the decreasing of photon number.

2. Reconstruction from simulated diffraction data

In order to determine the accuracy of the conventional BCDI algorithms, in this part, we reconstruct the nanoparticles based on the simulated noisy diffraction patterns and with the phase retrieval code from published work.[37] Similar to previous reports[34], in our work, we first use 10 iterations of the ER algorithm followed by 50 iterations of the RAAR.[24,26] (we have also used DM and HIO instead of RAAR with poorer results). We use 610 iterations in total so that the retrieval can end up with ER algorithm. More total iterations induce negligible changes while ending up with ER algorithm provides the best reconstruction. We apply a guided phase retrieval algorithm, which averages 5 random starts and repeats that for 3 generations.[38] With the retrieved information, we reconstruct the nanoparticles with different phase distribution. Figure 19 shows the reconstruction results from different magnitudes of

strain ε_0 of 10^{-4}, 10^{-3} and 10^{-2} and photon numbers n of 10^8, 10^6, and10^4. Each result in Figure 19 is an average of six reconstructions which we generated from different random starts, and we qualitatively inspect the reconstruction results by comparing with the input in Figure 18a_2.

For the low strain reconstructions shown in Figure 19b_1~19b_3, the phase retrieval correctly recovers the shape. Even for 10^4 photons, which is the lowest number of photons calculated, the shape reconstruction is still reasonable. However, for the stain field reconstruction in the low strain magnitude conditions, the oscillation in the strain field decreases the reliability of reconstruction. Figure 19b_1 still roughly has two distinguishable separate phases. However, a strong oscillation propagating along the lattice vector in the strain field significantly decreases the similarity between the reconstructed nanoparticle and the original one. In this condition, the maximal strain magnitude in this condition is over $3\varepsilon_0$, and the standard deviation reaches $6\varepsilon_0$. When the number of photons continues decreasing, the oscillation and the reliable reconstructed strain field mix up, and finally, the oscillation becomes dominant, as shown in Figure 19b_2~19b_3. The wavelength of these artefact strain oscillation also increases when the number of photons decreases. In Figure 19b_1, the oscillation is sharp, while in Figure 19b_2, some details, like the boundary of the two phases, are overwhelmed by the oscillation and become indistinguishable. In Figure 19b_3, the oscillation wavelength is even comparable to a quarter of the particle size.

For the intermediate strain where ε_0 equals to 10^{-3}, both shape reconstruction and strain field reconstructions are convincing if the number of photons is high enough, as shown in Figure 19d_1 and Figure 19d_2. We assume that this reliability is because their corresponding input Bragg peaks, shown in Figure c_1 and Figure c_2, begin to broaden

but not split yet. According to equation (7) and equation (9), the size of the Bragg peak is $2\pi/L$ ~ 1.256×10^{-2} nm^{-1}, and the distance between the peaks is 1.270×10^{-2} nm^{-1} when the strain magnitude is 10^{-3}. The distance between the two peaks is comparable to the size of the peaks. For Figure $19d_3$, the reconstruction fails due to the low photons number. In Figure $19c_3$, because the fringes become invisible, the algorithm likely regards the overlapped peaks as one broader peak, and thus the reconstruction is narrower than the original input along the *y*-axis. Although BCDI fails for the lowest photon numbers, BCDI performs best in the intermediate strain region simulated here. The flux available at today's synchrotron sources is sufficient and most of the reported literature reports strains in this range.

For the 10^{-2} high strain magnitude, conventional methods fail to reconstruct the nanoparticle even with high photon flux, as shown in Figure $19f_1$. The reconstruction in Figure $19f_1$ looks like the left part of nanoparticle with negative strain overlapping on the right part of the nanoparticle with positive strain. Traditional phase retrieval algorithms are unable to reconstruct the particle shape and seem to combine these two parts up within the wrong shape. We have also separated the diffraction pattern into two parts and applied traditional phase retrieval algorithms on each Bragg peak, respectively. The algorithms can separately reconstruct the two phases of the nanoparticle. However, this solution not only is unable to provide a convincing shape, it also lacks delivering the position and shape of the phase boundary in the nanoparticle. In summary, conventional algorithms fail to elucidate the evolution process of phase transformations if the strain is higher than about 1%, which is a common value in the lithium and sodium-ion intercalation materials.

In Figure 20 we show the average and the standard deviation of the strain calculated from six reconstructions from different random starts when ε_0 is 10^{-3} (see Figure 19c & 19d). The standard deviation is an estimate for the uncertainty of the BCDI method used here. It shows the different reconstruction results along the dashed line shown in Figure 19d. In the condition of 10^8 photons and 10^6 photons, the reconstruction results are both close to the original strain field while the standard deviations are also acceptable in both conditions. On the contrary, in the condition of 10^4 photons, only a part of the nanoparticle is reconstructed, and the strain in this condition is also lower than the original one.

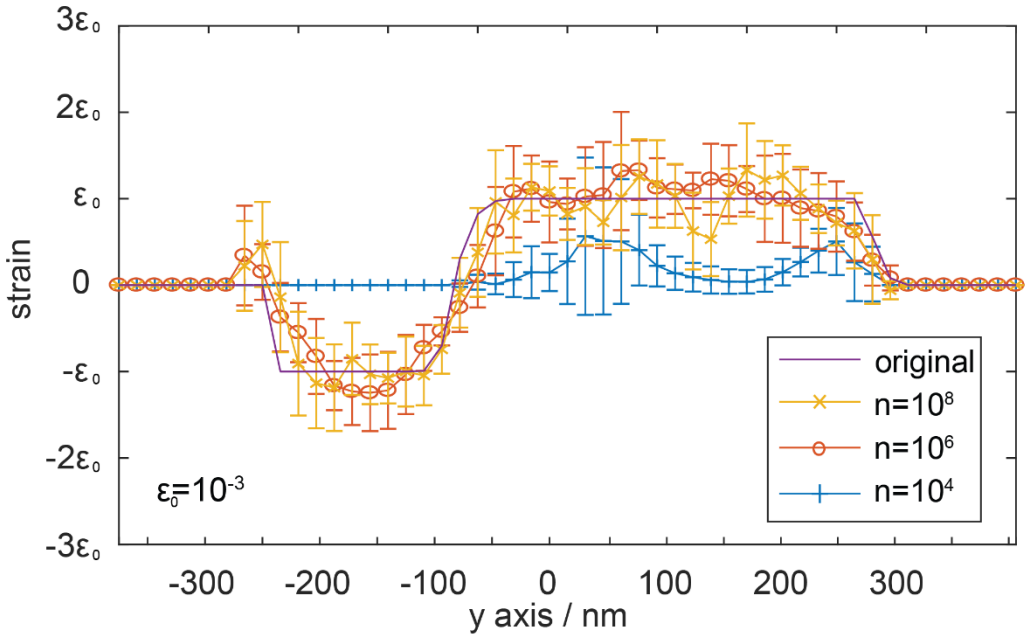

Figure 20. Strain fields around the *y*-axis reconstructed from diffraction patterns with different photon numbers and fixing strain magnitude as 10^{-3}. The figure shows an average strain field in the space 5 pixels around the *y*-axis. The standard deviation of 6 different reconstructions for each condition is also shown.

In Figure 20, when *y* is around -250 nm, the reconstructed strain increases to positive when the original strain disappears. This abnormal strain describes the positive strain on the left edge of the nanoparticle in Figure 19d_1 and Figure 19d_2. A hypothesis reason for this abnormal strain is the Gibbs phenomenon in Fourier transform. That is, when there is a jump discontinuity in periodic function, the Fourier series have large oscillations near this discontinuity.

3. Comparison of reconstruction with the original nanoparticles

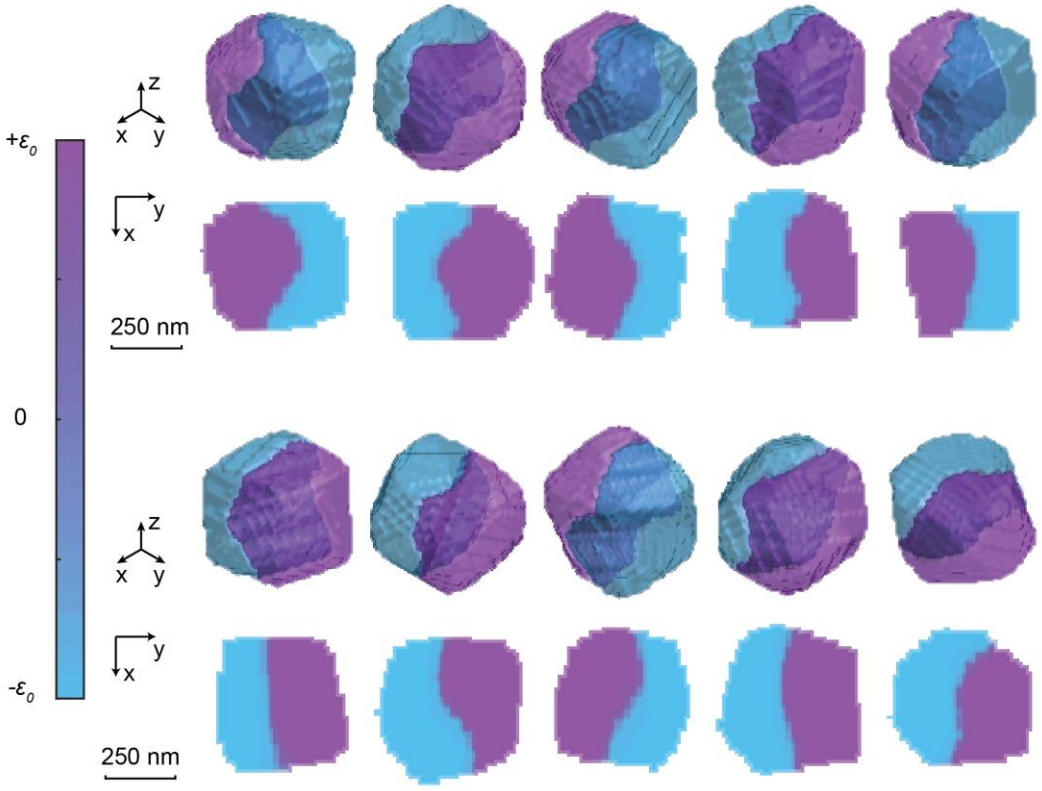

Figure 21. Simulated nanoparticles used for verifying the accuracy of the traditional reconstruction method.

For a quantitative evaluation of the reconstruction accuracy, we performed calculations on an ensemble of simulated nanoparticles with various shapes and various distribution of the phase boundary. We reconstructed diffraction patterns of 10 different 2-phases nanoparticles with the magnitude of strain varying from 10^{-5} to 10^{-2} and the photon number varying from 10^{8} to 10^{4}. These 10 nanoparticles are shown in Figure 21, and the one shown in Figure 18 is also included here. The simulation method for these nanoparticles is the same as the method for the nanoparticle shown in Figure 17(a).

Similar to previous publication[39], we quantify the similarity between the reconstructed nanoparticles and the original ones by calculating the error (E) between them. Here, the E is defined as:

$$\mathrm{E} = 2 \times \frac{\sum_{i=1}^{N^3} (\varepsilon - \varepsilon_0)^2}{\sum_{i=1}^{N^3} \varepsilon^2 + \sum_{i=1}^{N^3} \varepsilon_0^2} \tag{10}$$

Where ε is the reconstructed strain, ε_0 is the initial strain, and $N = 128$ is the number of pixels in one direction. By definition, $0 \leq \mathrm{E} \leq 4$. A smaller E represents a better reconstruction result. E = 0 only when the reconstruction finds the strain perfectly, and $\varepsilon = \varepsilon_0$ in all pixels. E = 4 only when the reconstruction is fully anticorrelated, and $\varepsilon = -\varepsilon_0$ in all pixels. As an example, the E of the strain field reconstructions in Figure 19d are 0.2218 (n=8), 0.3050 (n=6) and 1.7634 (n=4). We also use this method to evaluate the shape reconstruction result. The difference is that we compare the reconstructed shape function s with the original shape function s_0 shown in equation (7), instead of the strain ε and ε_0, as shown in equation (11). By qualitatively

comparing the reconstructions with the input, we determine that the shape of the phase coexistence and the strain value are reliable when E < 1.0.

$$\mathrm{E} = 2 \times \frac{\sum_{i=1}^{N^3}(s - s_0)^2}{\sum_{i=1}^{N^3} s^2 + \sum_{i=1}^{N^3} s_0^2} \tag{11}$$

The average E of the 10 nanoparticles in Figure 21 is shown in Figure 22a. Figure 22a$_1$ shows the strain field comparison, while Figure 22a$_2$ shows the shape function comparison. In Figure 22a$_1$ and Figure 22a$_2$, we divide the conditions into three parts: low strain ($\mathrm{n} + 6 \cdot \lg \varepsilon_0 < -13$), intermediate strain ($\mathrm{n} + 6 \cdot \lg \varepsilon_0 > -13$ & $\mathrm{n} - 6 \cdot \lg \varepsilon_0 < 23$), and high strain ($\mathrm{n} - 6 \cdot \lg \varepsilon_0 > 23$). This deviation is shown with white dash lines in Figure 22a.

For the low strain conditions in the low strain part, the strain field reconstruction hardly makes sense, but the shape reconstruction is reasonable. Typical reconstruction results are Figure 19b, where the oscillation appears in the strain field.

For an intermediate strain magnitude, both strain field reconstruction and shape reconstruction work well. Typical reconstruction results are Figure 19d$_1$ and Figure 19d$_2$. In this region, the distance between the two peaks is comparable to the size of the Bragg peak, as calculated. These conditions are in agreement of with literature, which successfully reconstruct the nanoparticle with BCDI.[32,33] When the ε_0 is around $10^{-2.75}$ to $10^{-3.00}$, the strain field reconstruction reaches its best, where the error E is lower than that of any other conditions once the number of photons is higher than 10^6.

For the high strain conditions, both shape reconstructions and strain field reconstructions are unreliable. Typical reconstruction results are Figure 19f$_1$ and Figure 19f$_1$. These reconstructions fail to arrange the two phases of the nanoparticle in the right positions, and the two phases overlap on each other.

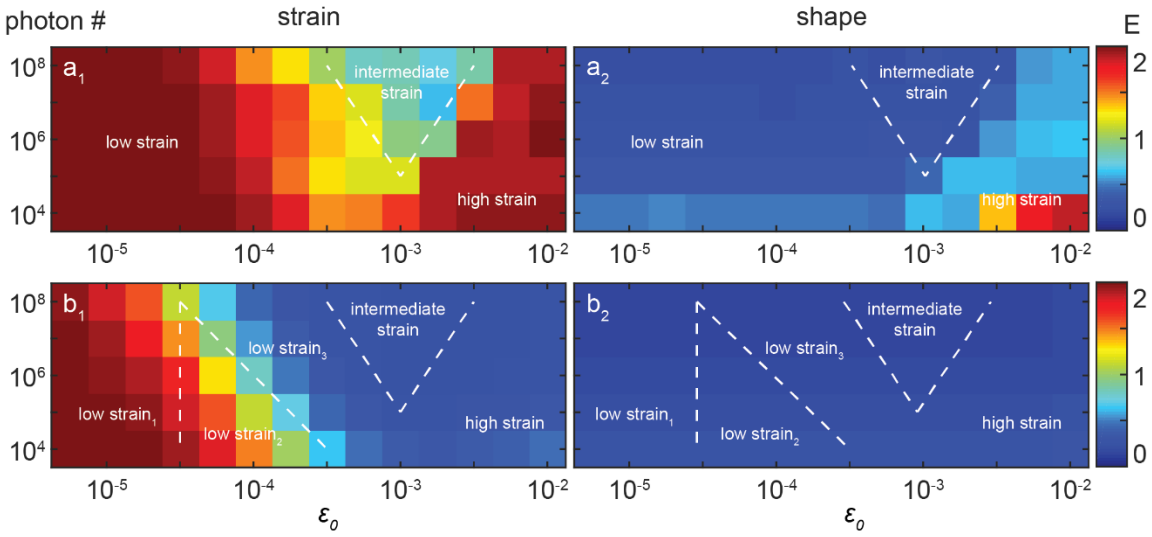

Figure 22. The average E of the strain field comparisons and the shape function comparisons of 10 different nanoparticles in different conditions. Column 1 shows the coefficient of the strain comparisons while column 2 only considers the shape function. Row a) shows the original situation. Row b) reconstructs the nanoparticle with the original phase angle of the light amplitude and the light intensity with Poisson noise. According to the definition of E, the blue part represents the satisfactory result and the red part means the reconstruction result is unreliable.

Poisson noise, detector resolution, and poor phase retrieval all may lead to inaccurate reconstructions. To discriminate the effect of these effects, we combine the noisy light intensity with the original phases and reconstruct the nanoparticle with a direct inverse Fourier transform. The E of these results is shown in Figure 22b. Compared with

Figure 22a, we further divide the left part into 3 parts: low strain$_1$ ($\lg \varepsilon_0 < -4.5$), low strain$_2$ ($\lg \varepsilon_0 > -4.5$ & $n + 4 \cdot \lg \varepsilon_0 < -10$), and low strain$_3$ ($n + 4 \cdot \lg \varepsilon_0 > -10$ & $n + 6 \cdot \lg \varepsilon_0 < -13$). This deviation is shown with white dash lines in Figure 22a.

For the low strain$_1$ part in Fig.22b, the main restriction is the resolution of the detector. The shifting of the peak is fully invisible in this situation. As we mentioned in section 2.1, when ε_0 is larger than $10^{-3.605}$, the centers of the split Bragg peaks locate in the same pixel, and we can only distinguish these peaks from the fringes. When the ε_0 continue decreasing, the fringes also overlap, which makes the phase retrieval unable to distinguish the peaks. In these conditions, we used phase retrieval on data without noise, but are still unable to reconstruct the strain field. Instead, random strain oscillation dominates the volume. This indicates a critical lower limit existing in the strain field reconstruction with BCDI. This lower limit varies with different experiment parameters. By increasing the size of the detector, we are able to lower this limitation.

For the low strain$_2$ part, even with fully retrieved phase angle, we are not able to provide a reasonable strain field reconstruction. In this region, the low photon number and the corresponding large noise are the main restrictions. For the last several visible fringes in these diffraction patterns, the intensities of them are relatively low. As the resolution of BCDI is closely related to the number of fringes, the strain field reconstruction in these conditions only has a limited resolution. This can be reflected from the strain oscillation with a long wavelength shown in Figure 19b$_3$. Although applied to a specific strain distribution, our results suggest that the strain sensitivity scales similarly to the spatial resolution. The slope of the dashed line in Figure 22b$_1$ is

about 4, suggesting the contrast scales with q^{-4}. Our results also show, that in the low strain region, even with a hypothetical perfectly working phase retrieval algorithm, the strain sensitivity decreases with decreasing signal due to noise.

For the left$_3$ part, compared with Figure 22a$_1$, the reconstruction with fully retrieved phase angle provides an accurate result. This means that in this region, both the Poisson noise and the poor phase retrieval are the reasons for the low E in Figure 22a$_1$. However, phase retrieval algorithms are never able to fully retrieval the phase angle from the noisy diffraction data. In these conditions, the ultimate of the retrieved phase angle is a good topic for future research. Here, we briefly simulate the ultimate phase retrieval result by adding random noise, ranging from $-\pi/\sqrt{10^n}$ to $+\pi/\sqrt{10^n}$, on the original phase angle. Here, this $1/\sqrt{10^n}$ is to simulate the signal-noise ratio of Poisson distribution. Compared with the result in Figure 22b$_1$, the decrease of E caused by the noisy phase angle is only in the magnitude of 0.01 in this region. Thus, if our simulated noisy phase angle can represent the ultimate phase retrieval result, then there is still enough room for the improvement of future phase retrieval algorithms in these conditions.

The biggest difference between Figure 22a and Figure 22b lies in the right part. With traditional phase retrieval algorithms, the reconstruction mixes both phases. We have tried to reconstruct the nanoparticle from the diffraction pattern without any noise, but the reconstruction still fails. However, with a fully retrieved phase, both strain field and particle shape are reconstructed with high accuracy even with a low photon number. This result indicates that with a better phase retrieval result, reconstructing the nanoparticle with large strain magnitude is possible.

In conclusion, with traditional phase retrieval algorithms, the strain field reconstruction reaches its best when the Bragg peak broadens but does not splits. Therefore, the critical requirement for a reliable strain field reconstruction is that the distance between two split peaks is comparable to the size of a single Bragg peak. This distance is in proportion to the magnitude of strain, while the size of the Bragg peak is inverse proportional to the size of the nanoparticle. In our simulation, for a nanoparticle with around $(500\ \text{nm})^3$ size, the critical strain magnitude for a convincing strain field reconstruction around $10^{-2.75}$ to $10^{-3.00}$. We show that the strain sensitivity decreases with decreasing photon number, even if the phase angle of the diffraction pattern is known. We also show that in for high strains the phase retrieval is the bottleneck: if the phases are known, it is possible to reconstruct the nanoparticle with high strain magnitude. Therefore, in the next chapter, we will upgrade traditional phase retrieval algorithms to enable us to reconstruct nanoparticles with the high strain magnitude.

CHAPTER 3

NOVEL ALGORITHM FOR PHASE TRANSITIONS WITH HIGH STRAIN

1. The principles of the new algorithm

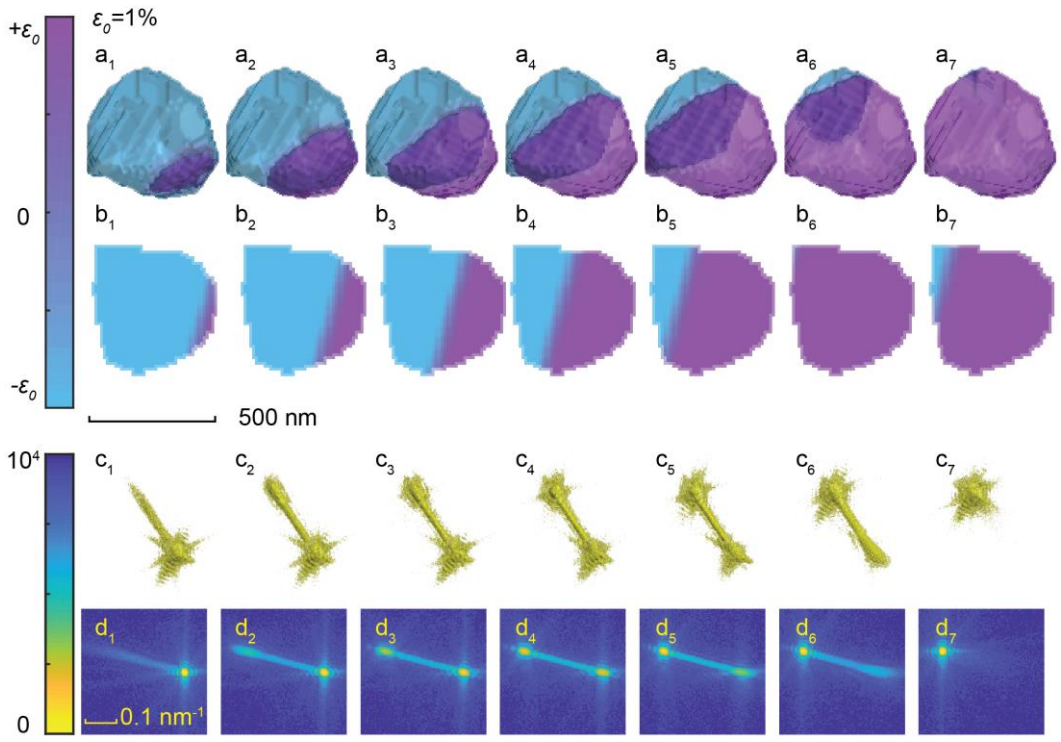

Figure 23. The simulated nanoparticle undergoing phase transformation and the corresponding simulated diffraction patterns in each state. From top to the bottom, we respectively show the 3D simulated nanoparticle, middle slices of the nanoparticle, 3D Bragg peaks and the projection of the Bragg peaks. The magnitude of strain is 1% and the number of photons is 10^6.

In Figure 19f$_1$, the reconstruction result shows that the current phase retrieval fails as the two structural phases spatially overlap. However, as shown in Figure 22b, using

the known complex phase of the diffraction pattern indicates that in the high strain situations reconstructing a reliable result is accessible, if the phase retrieval algorithm works. We have developed such an algorithm and will demonstrate it in the following paragraphs.

Our new algorithm based on using the multiple scans of the nanoparticle undergoing a phase transformation. Therefore, similar to the experiment shown in Figure 13, in Figure 23, we build a nanoparticle undergoing phase transformation process and simulate the corresponding diffraction patterns in 7 different states. Based on these multiple scans, the general process of this new algorithm is shown in Figure 24. Compared with traditional phase retrieval algorithms, our algorithm has several additional steps.

First, we reconstruct all 7 datasets simulated during the phase transition separately and then combine the shapes information of all 7 reconstructions. The motivation of this additional constrain is that, during the phase transformation process of the nanoparticle, like the LNMO nanoparticle in Figure 13, the shape of the nanoparticle hardly changes. That is because the phase transformation occurs thousands of times during the lifetime of the battery. More concretely, after the real space constraint, we calculate the average of the shape function of all 7 scans. Then for this average shape function, we regard values more than 0.6 as 1, while other values as 0. This operation is to fit the definition of shape function shown in section 1.3. For the n^{th} iteration, this function is marked as $\overline{S_{ns}}$ in Figure 24. In this end, we multiply this function on each of the shape functions. We do this operation for every 5 iterations.

Second, after the Fourier transform, reciprocal space constraint, and inverse Fourier transform, we smooth the support, marked as S_1^* in Figure 24, before the real space constraint. Traditional algorithms mix the two structural phases, and this overlapping leads to smaller support than the real shape function. This smooth function here can expand this support, and we apply this function for every iteration.

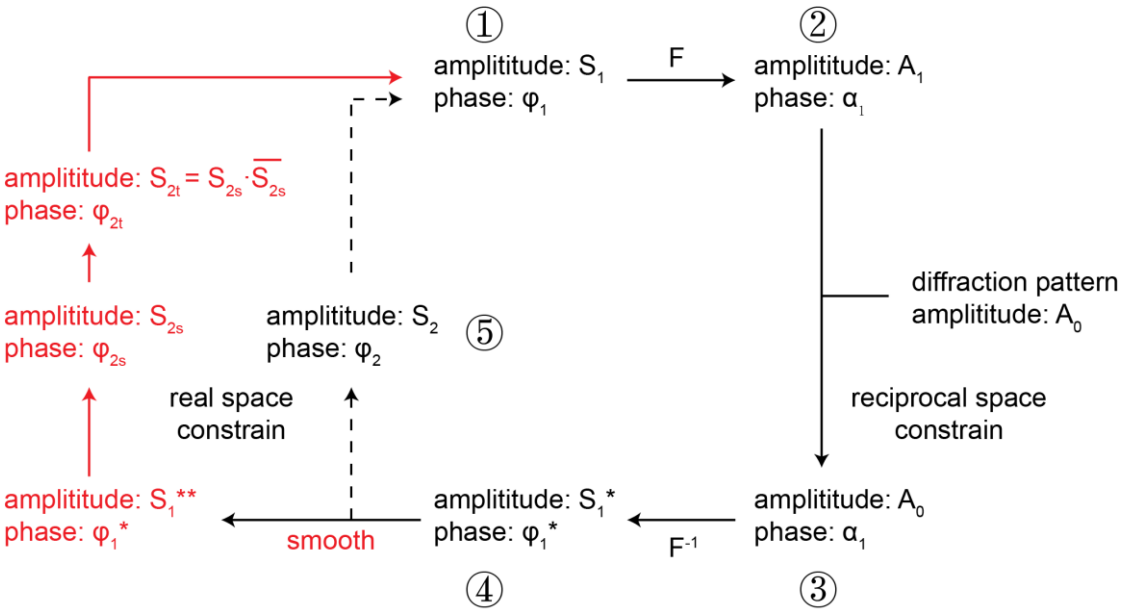

Figure 24. Schematically shows the phase retrieval process of our new algorithm. The black part is the traditional method and the red part is the innovation.

Third, we abandon the traditional guided algorithm. On the contrary, we run 30 different reconstructions from random starts for each particle. For every 5 iterations, we find the reconstructed result, which correlates the best with the other results by building a correlation matrix. Specifically, we calculate the error between two different reconstructions based on Equation (10). Then we sum up the error for each reconstruction and pick the one with the smallest total error. This method is similar to the correlation method used in Ref. 39.[40] Next, we find 4 other results most similar to

this reconstruction and average these five as the reconstruction result of this state in this iteration. As a flipped nanoparticle provides same diffraction pattern with the original one, we pick these 4 results from the other 29 original reconstructions and their corresponding flipped results.

In our work, we start with 10 iterations of traditional ER algorithm. Then we still use the new RAAR algorithm for 50 iterations and then use the new ER algorithm for 10 iterations. The three additional steps are applied in these 60 iterations in sequence. We repeat this 60 iterations loop for 10 times. Including the initial 10 iterations of traditional ER algorithm, we do 610 iterations in total, which is same with the method in Chapter 2.

2. Reconstruction with the new algorithm

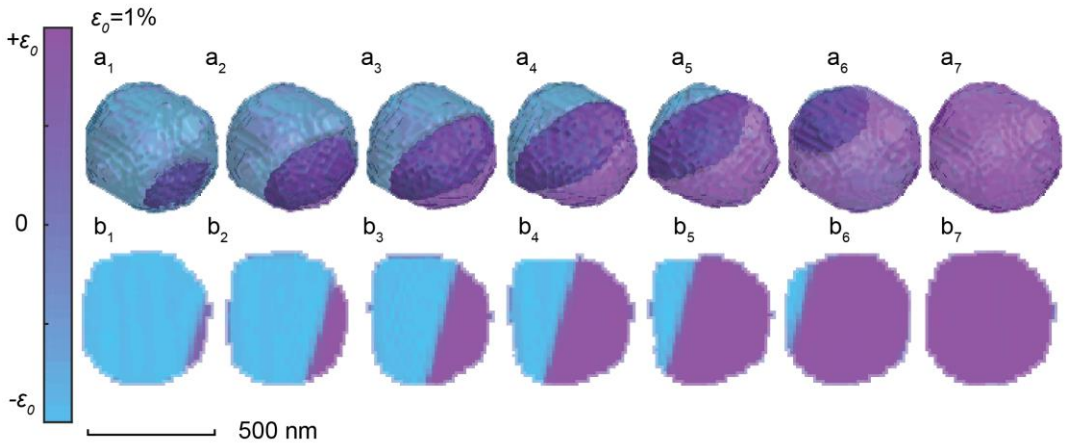

Figure 25. a) 3D reconstruction results with the new algorithm. b) Middle slices of the reconstructed nanoparticles.

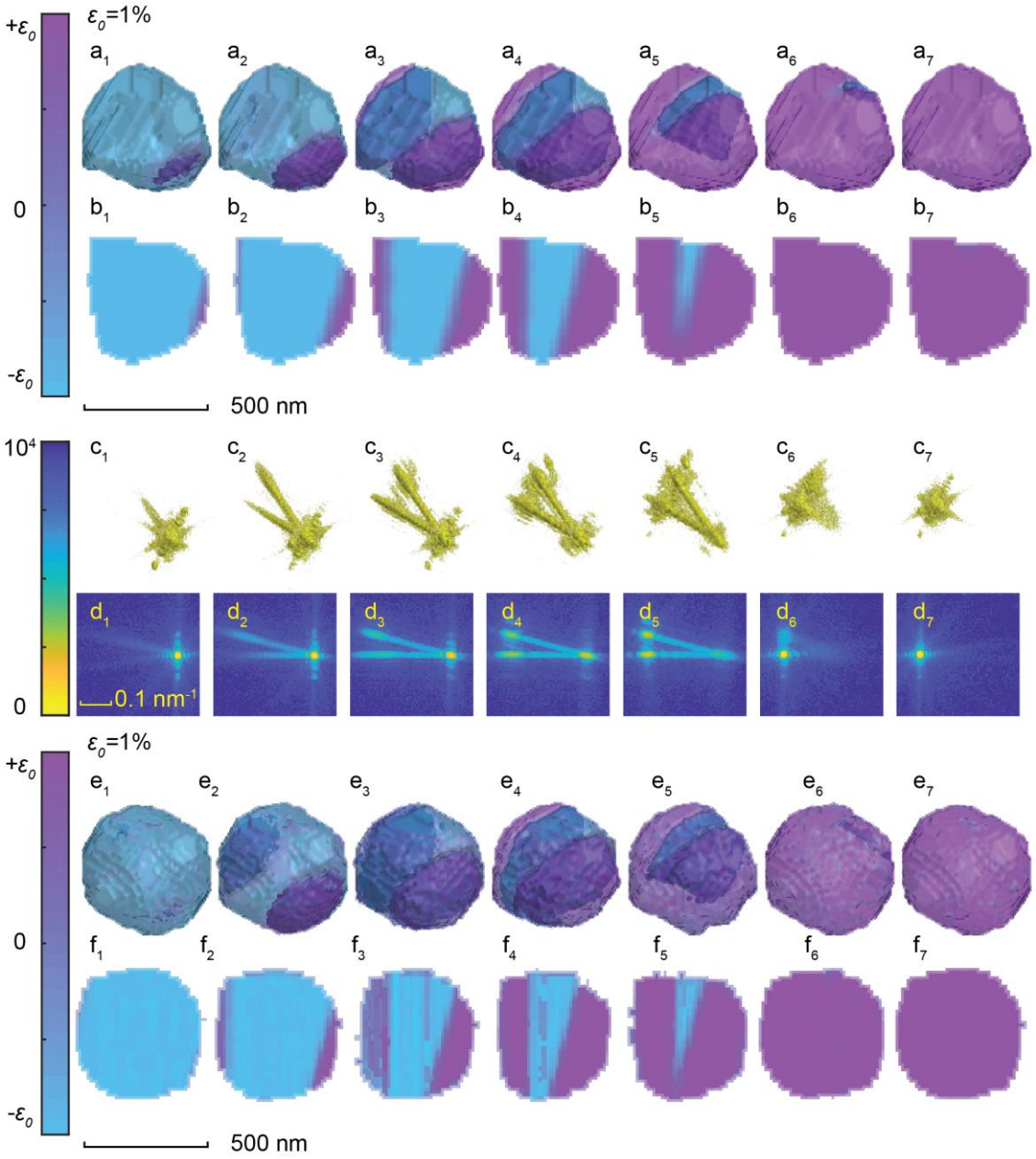

Figure 26. a) 3D simulated nanoparticle with phase transformations starting from both sides. b) Middle slices of the simulated nanoparticle. c) 3D simulated diffraction pattern. d) Projection of the diffraction pattern. e) 3D reconstruction results with the new algorithm. f) Middle slices of the reconstructed nanoparticles.

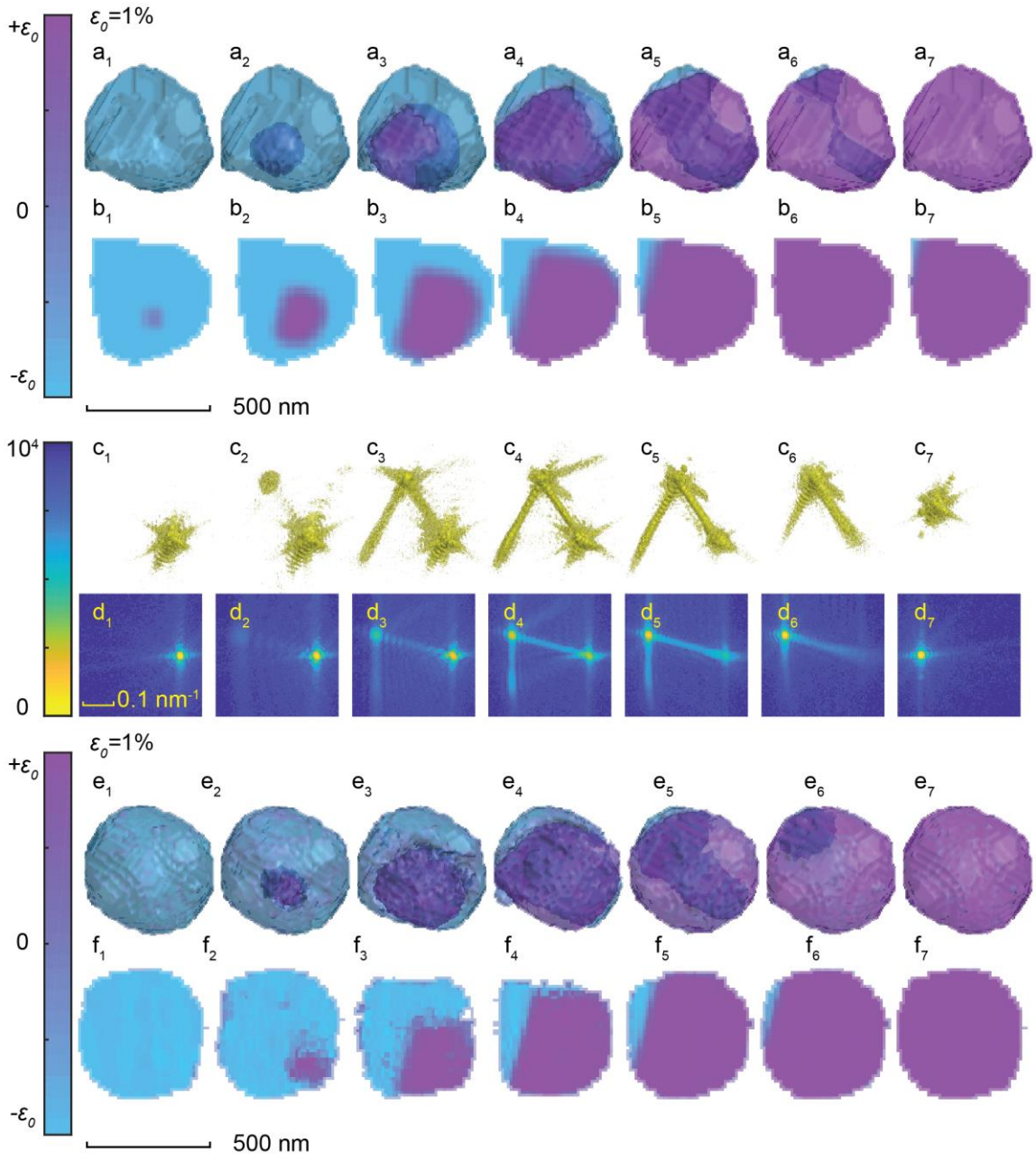

Figure 27. a) 3D simulated nanoparticle with phase transformations starting from inside. b) Middle slices of the simulated nanoparticle. c) 3D simulated diffraction pattern. d) Projection of the diffraction pattern. e) 3D reconstruction results with the new algorithm. f) Middle slices of the reconstructed nanoparticles.

Figure 25a and Figure 25b shows the reconstruction result of the nanoparticle shown in Figure 23 with our new algorithm. Compared with Figure 18f_2, our new algorithm fully reconstructs this nanoparticle with remarkably high reliability. The distribution of the two phases and the shape of this nanoparticle are both clearly shown. Except for the barely noticeable inaccuracies in reconstructing the shape of the particles, the reconstructions are virtually identical to the initial data.

In order to verify the generality of our new algorithm, with the methods shown in Figure 16, we distribute the different co-existing phases in two additional different ways. The original nanoparticles and the reconstruction results of these two distributions are shown in Figure 26 and Figure 27.

For these two situations, the nanoparticles are all reliably reconstructed. The different phases are distributed in their right positions, and the phase co-exists planes are all shown. The simulations were performed with an X-ray flux comparable with current achievable synchrotron sources. For all three phase coexistence examples we tried, the new algorithm we developed reliably reconstructs the phase coexistence in nanoparticles, opening a new avenue for studying phase transformation dynamics in functional nanomaterials.

3. Discussion on the new algorithm

Figure 28 shows the reconstruction result of the nanoparticle shown in Figure 23 with smooth function only and without multiplying the average. This result shows the role of the smooth function and the other steps in our new algorithm. For Figure 28a_3 and Figure 28a_4, when the two phases are comparable, the reconstruction is highly

convincing. It indicates that smooth function is capable of reconstructing two comparable phases with high strain magnitude. It can expand the size of reconstruction into a larger volume.

When the two phases have differences in size, like the situation for Figure 28a_1 and Figure 28a_6, the two phases are both reconstructed but are distributed in wrong positions. The minor phase also shows up in the flipped position. That is because the flipped input provides the same diffraction with the original input. As the minor phase is small, the correlating step has difficulties in distinguishing the flipped reconstruction and the original reconstruction. Therefore, the confinement with average shape function in our result becomes necessary. If we confine all these reconstruction results with the shape function in Figure 28a_4, this series of reconstructions are already highly convincing.

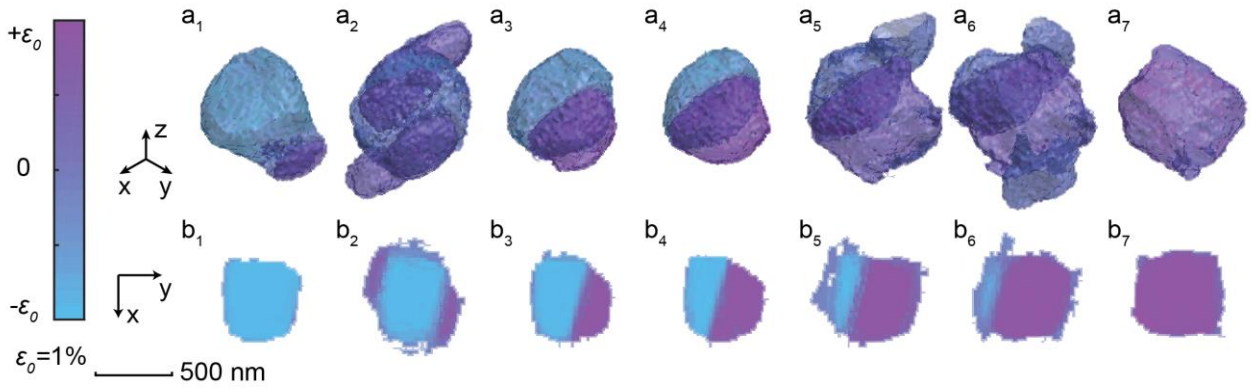

Figure 28. a) 3D reconstruction result without multiplying the average. b) The middle slices of the reconstructed nanoparticles in a).

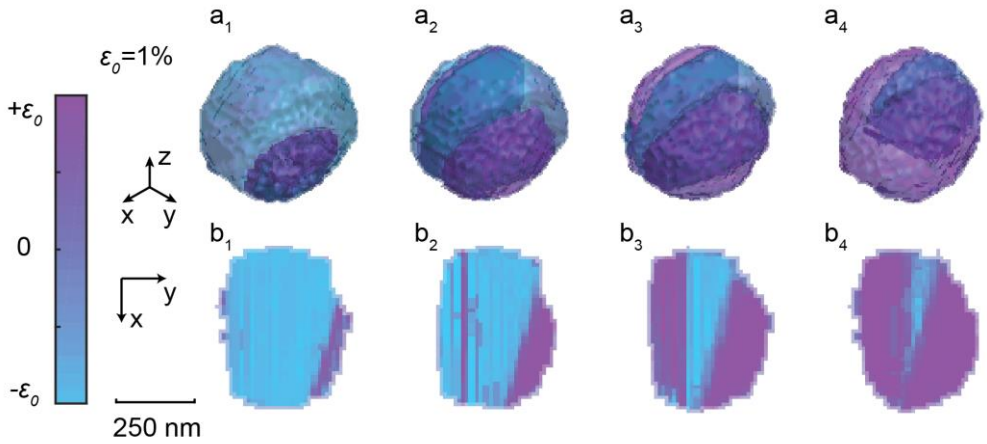

Figure 29. Reconstruction results from 4 scans of the simulated nanoparticle with phase transformations starting from both sides. The 3D reconstructions and the middle slices are respectively shown in a) and b).

Another aspect we investigated is how many scans are required for a successful reconstruction. In this thesis we used 7 scans. If we include fewer scans in the reconstruction, for some cases, the results are less reliable. As an example, Figure 29 shows the reconstruction results corresponding to the nanoparticles shown in Figure 26a_2 to Figure 26a_5. Compared with the reconstruction with 7 scans involved, these reconstruction results are smaller than the original nanoparticles. Particularly, for the reconstruction in Figure 29a_2, the left purple-colored phase almost disappears. This phenomenon is very similar to the reconstruction with traditional phase retrieval algorithms, which makes nanoparticle smaller. Therefore, it is beneficial to include additional diffraction scans of nanoparticle in the beginning or ending states of the phase transformation. These scans likely result in more convincing shape functions and benefit us in the first additional step mentioned in Section 3.1.

In conclusion, in this part, we have developed a new algorithm with strong capability in reconstructing the nanoparticle with a strain magnitude of 10^{-2}. We have verified

our result with different phase distributions. Our new algorithm is significantly useful in BCDI and gives future researcher a new possibility to study phase transformation.

CHAPTER 4

FUTURE WORK

For future research, we have several main prospects for future research.

First, in Figure 21, the low strain condition makes it impossible for strain field reconstruction. We also have the empirical approximation that, with the experiment parameters mentioned in Section 2.1, while $n + 4 \cdot \lg \varepsilon_0 < -10$, the reconstruction of the strain field only makes little sense. However, the physical reasons for this remain unclear. By revealing these reasons, we can better understand how Poisson noise affects the reconstruction results.

Second, our new algorithm has several improvement possibilities in detail that deserve research. Like the smooth function tends to make nanoparticle round. A higher reconstruction accuracy is achievable if the background problems are revealed and solved.

Third, we only verified the practicability of our algorithm with simulation data. We have tried our algorithm on some real experimental data of LNMO nanoparticles, and the preliminary results look promising. Our next step is applying our algorithm on a complete dataset of experimental data and help us better understand phase transformation processes.

CHAPTER 5

CONCLUSION

Based on the principles of Bragg coherent diffractive imaging, our project use simulation to reveal the accuracy of reconstruction phase coexistence in nanoparticle with the traditional phase retrieval algorithms. We change the magnitude of strain and the number of photons in the reciprocal space as two variables, and we set other parameters similar to real BCDI experiment.

In the low strain magnitude conditions, we reveal an empirical relationship that while $n + 4 \cdot \lg \varepsilon_0 < -10$, the reconstruction of the strain field hardly makes sense, even can fully retrieval the phase angle in the diffraction pattern. Our work also indicates a possible improvement possibility when $n + 4 \cdot \lg \varepsilon_0 > -10$ & $n + 6 \cdot \lg \varepsilon_0 < -13$ for future phase retrieval algorithms.

In the intermediate strain magnitude conditions, we find that the critical condition for a reliable strain field reconstruction is that the distance between the two peaks is comparable to the size of the Bragg peak. With the parameters we set, the most suitable strain magnitude is $10^{-2.75}$ to 10^{-3} for tradition phase retrieval algorithms.

In the high strain magnitude conditions, our work points out that traditional phase retrieval algorithms are unable to provide a convincing reconstruction result. In order to reconstruct the nanoparticle with a high magnitude of strain, we have developed a new phase retrieval algorithm. We succeed in reconstructing the nanoparticles with a 10^{-2} strain magnitude from their simulated diffraction data with a currently accessible

number of photons. We have also verified our algorithm with different types of phase distributions.

Our next step includes applying our algorithm on real experimental data. We hope our algorithm can help scientists better understand phase transformations when using Bragg coherent diffractive imaging.

REFERENCES

1. Gao, X., Cui, Y., Levenson, R. M., Chung, L. W. K. & Nie, S. In vivo cancer targeting and imaging with semiconductor quantum dots. *Nat. Biotechnol.* **22**, 969–976 (2004).
2. Liu, W.-T. Nanoparticles and their biological and environmental applications. *J. Biosci. Bioeng.* **102**, 1–7 (2006).
3. Murphy, C. J. *et al.* Anisotropic metal nanoparticles: Synthesis, assembly, and optical applications. *J. Phys. Chem. B* **109**, 13857–13870 (2005).
4. Lee, K. T. & Cho, J. Roles of nanosize in lithium reactive nanomaterials for lithium ion batteries. *Nano Today* **6**, 28–41 (2011).
5. Jiang, C., Hosono, E. & Zhou, H. Nanomaterials for lithium ion batteries. *Nano Today* **1**, 28–33 (2006).
6. Bruce, P. G., Scrosati, B. & Tarascon, J. Nanomaterials for Rechargeable Lithium Batteries. *Angew. Chemie Int. Ed.* **47**, 2930–2946 (2008).
7. Su, X. *et al.* Silicon-Based Nanomaterials for Lithium-Ion Batteries: A Review. *Adv. Energy Mater.* **4**, 1300882 (2014).
8. Ma, J., Hu, P., Cui, G. & Chen, L. Surface and Interface Issues in Spinel $LiNi_{0.5}Mn_{1.5}O_4$: Insights into a Potential Cathode Material for High Energy Density Lithium Ion Batteries. *Chem. Mater.* **28**, 3578–3606 (2016).
9. Yang, J., Han, X., Zhang, X., Cheng, F. & Chen, J. Spinel $LiNi_{0.5}Mn_{1.5}O_4$ cathode for rechargeable lithiumion batteries: Nano vs micro, ordered phase $P4_332$ vs disordered phase $Fd\bar{3}m$. *Nano Res.* **6**, 679–687 (2013).
10. Cabana, J. *et al.* Composition-Structure Relationships in the Li-Ion Battery Electrode Material $LiNi_{0.5}Mn_{1.5}O_4$. *Chem. Mater.* **24**, 2952–2964 (2012).
11. Xiao, J. *et al.* High-Performance $LiNi_{0.5}Mn_{1.5}O_4$ Spinel Controlled by Mn^{3+}

Concentration and Site Disorder. *Adv. Mater.* **24**, 2109–2116 (2012).

12. Kim, J.-H., Myung, S.-T., Yoon, C. S., Kang, S. G. & Sun, Y.-K. Comparative Study of $LiNi_{0.5}Mn_{1.5}O_{4-\delta}$ and $LiNi_{0.5}Mn_{1.5}O_4$ Cathodes Having Two Crystallographic Structures: $Fd\bar{3}m$ and $P4_332$. *Chem. Mater.* **16**, 906–914 (2004).
13. Wang, L., Li, H., Huang, X. & Baudrin, E. A comparative study of $Fd\bar{3}m$ and $P4_332$ "$LiNi_{0.5}Mn_{1.5}O_4$". *Solid State Ionics* **193**, 32–38 (2011).
14. Lee, E. & Persson, K. A. Revealing the coupled cation interactions behind the electrochemical profile of $Li_xNi_{0.5}Mn_{1.5}O_4$. *Energy Environ. Sci.* **5**, 6047–6051 (2012).
15. Kim, J.-H., Yoon, C. S., Myung, S.-T., Prakash, J. & Sun, Y.-K. Phase Transitions in $Li_{1-\delta}Ni_{0.5}Mn_{1.5}O_4$ during Cycling at 5 V. *Electrochem. Solid-State Lett.* **7**, A216 (2004).
16. Kim, J. H. *et al.* Understanding the capacity fading mechanism in $LiNi_{0.5}Mn_{1.5}O_4$/graphite Li-ion batteries. *Electrochim. Acta* **90**, 556–562 (2013).
17. Daniel, I. M. & Ishai, O. Engineering mechanics of composite materials. *Mater. Des.* **17**, 114 (1996).
18. Vartanyants, I. A; Robinson, I. K. Partial coherence effects on the imaging of small crystals using coherent x-ray diffraction. *J. Phys. Condens. Matter* **13**, 10593–10611 (2001).
19. Boulet-Roblin, L. *et al.* Operando Neutron Powder Diffraction Using Cylindrical Cell Design: The Case of $LiNi_{0.5}Mn_{1.5}O_4$ vs Graphite. *J. Phys. Chem. C* **120**, 17268–17273 (2016).
20. Als-Nielsen, J. & McMorrow, D. *Elements of Modern X-ray Physics*. *Elements of Modern X-ray Physics* (John Wiley & Sons, Inc., 2011).
21. Robinson, I. & Harder, R. Coherent X-ray diffraction imaging of strain at the

nanoscale. *Nat. Mater.* **8**, 291–298 (2009).

22. Williams, G. J., Pfeifer, M. A., Vartanyants, I. A. & Robinson, I. K. Three-Dimensional Imaging of Microstructure in Au Nanocrystals. *Phys. Rev. Lett.* **90**, 4 (2003).
23. Gerchberg, R. W. & Saxton, W. O. A practical algorithm for the determination of phase from image and diffraction plane pictures. *Optik (Stuttg).* **35**, 237–246 (1972).
24. Fienup, J. R. Phase retrieval algorithms: a comparison. *Appl. Opt.* **21**, 2758–2769 (1982).
25. Elser, V. Phase retrieval by iterated projections. *J. Opt. Soc. Am. A* **20**, 40 (2003).
26. Luke, D. R. Relaxed averaged alternating reflections for diffraction imaging. *Inverse Probl.* **21**, 37–50 (2005).
27. Robinson, I. K., Vartanyants, I. A., Williams, G. J., Pfeifer, M. A. & Pitney, J. A. Reconstruction of the shapes of gold nanocrystals using coherent x-ray diffraction. *Phys. Rev. Lett.* **87**, 1–4 (2001).
28. Ulvestad, A., Clark, J. N., Harder, R., Robinson, I. K. & Shpyrko, O. G. 3D Imaging of Twin Domain Defects in Gold Nanoparticles. *Nano Lett.* **15**, 4066–4070 (2015).
29. Clark, J. N. *et al.* Three-dimensional imaging of dislocation propagation during crystal growth and dissolution. *Nat. Mater.* **14**, 780–784 (2015).
30. Ulvestad, A. *et al.* Topological defect dynamics in operando battery nanoparticles. *Science (80-.).* **348**, 1344–1347 (2015).
31. Singer, A. *et al.* Nonequilibrium structural dynamics of nanoparticles in $LiNi_{0.5}Mn_{1.5}O_4$ cathode under operando conditions. *Nano Lett.* **14**, 5295–5300 (2014).

32. Ulvestad, A. *et al.* In situ strain evolution during a disconnection event in a battery nanoparticle. *Phys. Chem. Chem. Phys.* **17**, 10551–10555 (2015).
33. Ulvestad, A. *et al.* Correction to Single Particle Nanomechanics in Operando Batteries via Lensless Strain Mapping. *Nano Lett.* **15**, 3654–3654 (2015).
34. Singer, A. *et al.* Nucleation of dislocations and their dynamics in layered oxide cathode materials during battery charging. *Nat. Energy* **3**, 641–647 (2018).
35. Ulvestad, A. *et al.* Topological defect dynamics in operando battery nanoparticles. *Science (80-.).* **348**, 1344–1347 (2015).
36. Cahn, J. W. On spinodal decomposition. *Acta Metall.* **9**, 795–801 (1961).
37. Marchesini, S. A unified evaluation of iterative projection algorithms for phase retrieval. *Rev. Sci. Instrum.* **78**, (2007).
38. Chen, C. C., Miao, J., Wang, C. W. & Lee, T. K. Application of optimization technique to noncrystalline x-ray diffraction microscopy: Guided hybrid input-output method. *Phys. Rev. B - Condens. Matter Mater. Phys.* **76**, 1–5 (2007).
39. Clark, J. N., Huang, X., Harder, R. & Robinson, I. K. High-resolution three-dimensional partially coherent diffraction imaging. *Nat. Commun.* **3**, 993–996 (2012).
40. Vine, D. *et al.* Domain morphology, boundaries, and topological defects in biophotonic gyroid nanostructures of butterfly wing scales. *Sci. Adv.* **2**, e1600149 (2016).